

**AEROELASTIC ANALYSIS OF AIRCRAFT:
WING AND WING/FUSELAGE CONFIGURATIONS**

by

**H. H. Chen, K. C. Chang, T. Tzong, and T. Cebeci
Advanced Transport Aircraft Systems
McDonnell Douglas Corporation**

May 1997

**Prepared Under
Contract No. NAS2-14091
for
NASA Ames Research Center**

Summary

A previously developed interface method for coupling aerodynamics and structures is used to evaluate the aeroelastic effects for an advanced transport wing at cruise and under-cruise conditions. The calculated results are compared with wind tunnel test data. The capability of the interface method is also investigated for an MD-90 wing/fuselage configuration. In addition, an aircraft trim analysis is described and applied to wing configurations.

The accuracy of turbulence models based on the algebraic eddy viscosity formulation of Cebeci and Smith is studied for airfoil flows at low Mach numbers by using methods based on the solutions of the boundary-layer and Navier-Stokes equations.

1.0 INTRODUCTION

The aeroelastic analysis of an aircraft requires an accurate and efficient procedure to couple aerodynamics and structures. This procedure can be developed by using either a closely coupled approach in which the aerodynamic and structural equations are solved simultaneously, or a loosely coupled one, in which the loads computed with an aerodynamic model are transformed into a structural model for structural analysis, and the displacements resulting from the structural analysis are converted back to the aerodynamic model to update the geometry. The advantage of the closely coupled approach is that the results can be obtained with a single analysis. However, an extensive code modification is required to couple any structural and aerodynamic codes and, hence, the evaluation of a new structural or aerodynamic code may be time-consuming and costly. On the contrary, at a cost of a few iterations between aerodynamic and structural models to get converged solutions for loads and displacements, a general interaction procedure using the loosely coupled approach can be established. Using this procedure, the aeroelastic analysis can be conducted with any aerodynamic and structural codes with little modifications to either code.

In structural design, the aeroelastic analysis is usually performed with a crude aerodynamic model using linear aerodynamic methods such as the vortex lattice method and a high fidelity structural model. In the aerodynamic performance evaluation, a high fidelity aerodynamic model using advanced aerodynamic codes along with a crude structural model is employed. While both approaches can provide an accurate prediction of total loads, lift and drag for the entire aircraft, they may not provide accurate prediction of loads on aircraft components such as flaps, slats and spoilers. As a result, it is necessary to conduct flight tests. Furthermore, in structural design, the local loads (loads at finite element nodal points) are distributed from global loads according to a presumed pressure distribution. The global loads including shear, moment and torque at each wing section are computed using a simple beam model. Therefore, the local loads may not be accurate. For these reasons, an interface method, which is suitable for both loads and performance evaluation of the entire aircraft as well as aircraft components and conserves local and global loads, is desirable.

In the first phase of the present contract, an interface method satisfying the above requirements and using a loosely coupled approach was developed [1]. The interface method was general in the sense that the loads computed by any aerodynamic code can be transformed to the finite element (FE) model and the displacements from the FE model to the aerodynamic model. This was demonstrated by applying the method to wings at subsonic and transonic flow conditions.

In the present report we extend our studies to wing/fuselage configurations and use the interface method to conduct aircraft trim analysis. After a brief description of the interface method in Section 2, we apply the method to an advanced transport wing at cruise and under-cruise conditions. Using the parallel version of the OVERFLOW code

[2] to compute the aerodynamic loads and a McDonnell Douglas finite element code to perform structural analysis, the aeroelastic effects are determined for this wing and the calculated results are compared with the experimental data described in Section 3.

The application of the interface method to wing/fuselage configurations is discussed in Section 4. An MD-90 wing/fuselage configuration is chosen for this purpose. Again, the parallel version of the OVERFLOW code on IBM SP-2 was used to compute the pressure distributions on the surface of the MD-90 wing/fuselage.

Aircraft trim analysis is used to determine the angle of attack and deflection of control surfaces for structural loads calculation as well as performance evaluation. In production, the analysis is usually conducted by linear aerodynamic methods such as the vortex lattice method with an assumption that the aircraft deflection is a linear combination of pre-selected vibration modal shapes. This production analysis, however, does not include the nonlinearity of aerodynamics and relies on wind tunnel test data to correct the results. With the interface method, more accurate trim analysis can be performed with advanced aerodynamic codes in which the nonlinear aerodynamic effects are included. This is demonstrated in Section 5 for a simple wing configuration at transonic flow conditions.

In Section 6, we describe the extension of our studies to high-lift configurations. Since the interface method is a general one in the sense that any aerodynamic code can be used to calculate the loads, preliminary studies are under way to compute loads with the Douglas Neumann code developed by J. Hess [3]. The geometry being considered for this study is the MD-90 high-lift configuration. This work will be the basis for phase three of the present contract.

The advanced aerodynamic codes used to calculate loads for finite-element methods require turbulence models which need to be accurate to make the loads-calculations accurate. While there are several models that can be used for this purpose, and while most of these models are satisfactory for attached flows, they are not so satisfactory for separated flows. In Section 7, we consider a popular algebraic eddy viscosity formulation due to Cebeci and Smith [4] and its different versions and investigate their accuracy for predicting the performance of airfoils at low Mach numbers for a wide range of angles of attack, including stall and post stall. The models include the Baldwin-Lomax model [5], the original CS model with length scale recommendations due to Stock and Haase [6] and Johnson [7], the Johnson and King (JK) model [8], and a modified CS model due to Cebeci and Chang [9]. We use these models in methods based on interactive boundary layer and Navier-Stokes methods and compare the calculated results with experimental data.

The report ends with conclusions and recommendations in Section 8.

2.0 INTERFACE METHOD

A general interface method must be able to take into account of the different characteristics between aerodynamic and structural models in order to convert the loads and deformations between the two models. The aerodynamic model generally includes details of the aircraft geometry, such as flaps, slats, pylon, nacelle, etc., and closely resembles to the true geometry of the aircraft. However, the structural finite element model usually represents only major structural components. For example, the wing box, which carries major loads in the spanwise direction, is of main structural concern and modeled in reasonable detail. The flaps and slats, which carry relatively small loads, are either represented by simple beam elements or completely excluded from the finite element model. In addition, engine and pylon are usually modeled by a lumped (point) mass element and a general stiffness matrix, respectively, which do not resemble the true configurations of the components at all. Furthermore, tens of thousands aerodynamic grid points on the surface of an aircraft are usually needed to compute the pressure distribution. However, only hundreds or thousands of finite element nodal points are used to model aircraft structures. The difference in fidelity results in gaps between the aerodynamic and the finite element models. In order to accurately convert the loads and displacements, the difference between the two models must be considered in the interface method.

A general interface method that fulfills the above requirements was developed in the first phase of the present contract [1]. This method is based on finite element (FE) technology in which virtual work is employed to transform aerodynamic pressures into FE nodal forces. The displacements at FE nodes are then converted back to aerodynamic grid points on the aircraft surface through the reciprocal theorem in structural engineering. The conversion of loads between the aerodynamic and FE models is accomplished by integrating pressures on the aerodynamic model rather than transforming the pressures directly to the FE model. The reason for this choice is because the surface area of the FE model does not represent the aircraft geometry accurately.

The first step in performing the aeroelastic analysis with the interface method is to project each aerodynamic grid point on the aircraft surface onto an adjacent finite element. The projection generates basic data which are needed in the aero-structure interaction process. The data include the finite element projected by each aerodynamic grid point, the projected location of the aerodynamic grid point on the element and the offset distance from the aerodynamic grid point to the element surface. With this information, the displacements at an aerodynamic grid point on the aircraft surface are expressed in terms of the displacements at the projected location on the finite element surface as

$$\underline{u}_{aero} = \begin{Bmatrix} u \\ v \\ w \end{Bmatrix}_{aero} = \begin{bmatrix} 1 & 0 & 0 & 0 & r_z & 0 \\ 0 & 1 & 0 & -r_z & 0 & 0 \\ 0 & 0 & 1 & 0 & 0 & 0 \end{bmatrix} \begin{Bmatrix} u \\ v \\ w \\ \theta_x \\ \theta_y \\ \theta_z \end{Bmatrix}_{FE} \quad (1)$$

where \underline{u}_{aero} contains three translational displacement components at the aerodynamic grid point, and r_z is the offset distance from the aerodynamic grid point to the element surface. The finite element displacements include both the translational degrees of freedom (DOF) u, v and w and rotational DOF θ_x, θ_y and θ_z . However, membrane elements that are commonly used to represent skin, ribs and spars of aircraft wings do not have any rotational DOF at the finite element nodal points. To determine the rotations at the projected location, they are expressed by the differentials of the translational displacements as

$$\begin{Bmatrix} \theta_x \\ \theta_y \\ \theta_z \end{Bmatrix}_{FE} = \frac{1}{2} \begin{bmatrix} 0 & -\frac{\partial}{\partial z} & \frac{\partial}{\partial y} \\ \frac{\partial}{\partial z} & 0 & -\frac{\partial}{\partial x} \\ -\frac{\partial}{\partial y} & \frac{\partial}{\partial x} & 0 \end{bmatrix} \begin{Bmatrix} u \\ v \\ w \end{Bmatrix}_{FE} \quad (2)$$

The displacements at each aerodynamic grid point are then expressed in terms of the translational displacements at the projected location as

$$\underline{u}_{aero} = \frac{1}{2} \begin{bmatrix} 1 & 0 & 0 & 0 & r_z & 0 \\ 0 & 1 & 0 & -r_z & 0 & 0 \\ 0 & 0 & 1 & 0 & 0 & 0 \end{bmatrix} \begin{bmatrix} 2 & 0 & 0 \\ 0 & 2 & 0 \\ 0 & 0 & 2 \\ 0 & -\frac{\partial}{\partial z} & \frac{\partial}{\partial y} \\ \frac{\partial}{\partial z} & 0 & -\frac{\partial}{\partial x} \\ -\frac{\partial}{\partial y} & \frac{\partial}{\partial x} & 0 \end{bmatrix} \begin{Bmatrix} u \\ v \\ w \end{Bmatrix}_{FE} \quad (3)$$

By employing the reciprocal theorem, forces and moments at the projected location on the finite element surface are written in terms of forces at the aerodynamic grid point as

$$\underline{p}_{FE} = \begin{Bmatrix} p_x \\ p_y \\ p_z \\ m_x \\ m_y \\ m_z \end{Bmatrix}_{FE} = \begin{bmatrix} 1 & 0 & 0 \\ 0 & 1 & 0 \\ 0 & 0 & 1 \\ 0 & -r_z & 0 \\ r_z & 0 & 0 \\ 0 & 0 & 0 \end{bmatrix} \begin{Bmatrix} p_x \\ p_y \\ p_z \end{Bmatrix}_{aero} \quad (4)$$

where \underline{p}_{FE} is the force vector on the finite element surface and $\underline{p}_{aero} = \begin{Bmatrix} p_x & p_y & p_z \end{Bmatrix}_{aero}^T$ is the force at the aerodynamic grid point obtained by integrating aerodynamic pressures over the area surrounding the point. In the above equation, the moments due to the offset distance r_z from the aerodynamic grid point to the element surface and the inplane force components p_x and p_y are conserved. In addition, the offset can properly transform the aerodynamic forces on aircraft components that are excluded from the finite element model.

2.1 Finite Element Forces by Virtual Work

The virtual work in the finite element formulation can be expressed as

$$W = \int \delta \underline{u}_{FE}^T \underline{p}_{FE} dA = \delta \underline{U}^T \underline{F} \quad (5)$$

where W is the virtual work, \underline{p}_{FE} and \underline{u}_{FE} are the load and displacement vectors at any point on the element surfaces, and A is the surface area of the structure subjected to aerodynamic pressures. $\underline{u}_{FE} = \{u \ v \ w \ \theta_x \ \theta_y \ \theta_z\}_{FE}^T$ contains both the translational and rotational displacement components. \underline{F} and \underline{U} are the finite element nodal forces and displacements, respectively.

With the introduction of the finite element shape functions, the translational displacements at any location on the element surface can be written as

$$\underline{\bar{u}}_{FE} = \underline{N} \underline{U} = \sum_i \begin{bmatrix} N_i & 0 & 0 \\ 0 & N_i & 0 \\ 0 & 0 & N_i \end{bmatrix} \begin{Bmatrix} U \\ V \\ W \end{Bmatrix}_i \quad (6)$$

The rotations at any location are given by

$$\underline{\bar{\theta}}_{FE} = \nabla \underline{N} \underline{U} = \frac{1}{2} \sum_i \begin{bmatrix} 0 & -\frac{\partial N_i}{\partial z} & \frac{\partial N_i}{\partial y} \\ \frac{\partial N_i}{\partial z} & 0 & -\frac{\partial N_i}{\partial x} \\ -\frac{\partial N_i}{\partial y} & \frac{\partial N_i}{\partial x} & 0 \end{bmatrix} \begin{Bmatrix} U \\ V \\ W \end{Bmatrix}_i \quad (7)$$

where \underline{N} is the matrix of the element shape functions, $\nabla \underline{N}$ is the differential of the shape functions \underline{N} and $\{U \ V \ W\}_i^T$ are the displacements at the i th node of the finite element model.

With Eqs. (6) and (7), Eq. (5) can be written as

$$\underline{W} = \delta \underline{U}^T \left[\int \left(\underline{N}^T \underline{\bar{p}}_{FE} + \nabla \underline{N}^T \underline{\bar{m}}_{FE} \right) dA \right] \quad (8)$$

where $\underline{\bar{p}}_{FE} = \{p_x \ p_y \ p_z\}^T$ and $\underline{\bar{m}}_{FE} = \{m_x \ m_y \ m_z\}^T$ denote the distributed forces and moments at any location on the element surface, respectively.

From Eqs. (5) and (8), the finite element nodal forces are found to be

$$\underline{F} = \int \left(\underline{N}^T \underline{\bar{p}}_{FE} + \nabla \underline{N}^T \underline{\bar{m}}_{FE} \right) dA \quad (9)$$

In terms of forces and moments projected from the aerodynamic grid point to the finite element surface, the above equation can be written as

$$\underline{F} = \sum_{j=1}^M \left(\underline{N}^T(\xi_j, \eta_j) \underline{\bar{p}}_{FE_j} + \nabla \underline{N}^T(\xi_j, \eta_j) \underline{\bar{m}}_{FE_j} \right) \quad (10)$$

where ξ_j and η_j denote the coordinates of the projected location of the j th aerodynamic grid point on a finite element, $\underline{\bar{p}}_{FE_j}$ and $\underline{\bar{m}}_{FE_j}$ denote the corresponding finite element forces and moments converted from the aerodynamic point forces by Eq. (4), and M denote the total number of aerodynamic grid points on the aircraft surface.

After the load vector is formed, the displacements at finite element nodes can be obtained with structural analysis. The displacements at aerodynamic grid points are then computed by Eq. (3).

2.2 Iteration Procedure

To perform the aero-structure interaction, the aerodynamic loads on the undeformed wing are first calculated and applied to the finite element model in order to compute the elastic deformation. A modified wing geometry is then obtained by superimposing the elastic deformation on the original wing geometry. The next iteration is performed by calculating the aerodynamic loads based on the modified wing geometry due to elastic deformation. If the deformation is small, the stiffness of the finite element model only changes slightly with the geometry and it could be assumed that the stiffness of the deformed wing remains the same as that of the undeformed wing. Based on this assumption, the aerodynamic loads on the modified wing geometry are applied to the original finite element model in order to compute a new elastic deformation. This deformation is again superimposed on the undeformed wing to determine an updated wing geometry for the next iteration. This procedure is repeated until both loads and deformations converge. An underrelaxation parameter is often used to expedite the convergence of the iteration.

2.3 Grid Perturbation for Deformed Geometry

One of the major problems of computational fluid dynamics (CFD) in solving the Euler/Navier-Stokes equations lies in the area of grid generation which can be tedious and labor-intensive, requiring hours or days of work even for relatively simple configurations. For aeroelastic analysis, iterations between the aerodynamic and structural models are required to get converged solutions for both loads and deformations. To generate a new grid for the deformed geometry at every iteration can involve substantial work which may not be practical and acceptable. To minimize the effort, a grid perturbation technique for moving grids is desirable for the aeroelastic calculations.

A grid perturbation code, CSCMDO, developed by Jones & Samareh-Abolhassani [10] at NASA Langley, was adopted for this purpose. This code generates a new grid for the deformed geometry by perturbing the original grid (i.e. the grid for the undeformed geometry) such that the surface of the new field grid coincides with the surface of the deformed geometry. It is applicable as long as the movements of the deformed surface are small so that the original grid topology is not violated. The code can be used for grid systems with either single or multiple blocks.

CSCMDO can be used to generate grids to solve either the Euler or Navier-Stokes equations. For the latter, care must be taken to satisfy the requirement of extremely fine grid spacing near the wall. This makes the grid perturbation a difficult task. For complex geometries such as the MD-90 wing/fuselage configuration, the grid perturbation code is not capable of generating the Navier-Stokes grid for the deformed geometry. For this reason, the code is first used to generate the Euler grid which allows coarser grid spacing

near the wall. The perturbed Euler grid is then adjusted to satisfy the grid requirements for Navier-Stokes calculations.

3.0 VALIDATION AND EVALUATION OF THE INTERFACE METHOD

To validate the aero-structure interface method, static aeroelastic analysis was performed on an advanced McDonnell Douglas transport wing model for which extensive wind tunnel data are available. This model [5] is a 2.426 percent scale representation of the original advanced transonic transport configuration, MD-12. The wind tunnel tests were conducted at the NASA Langley National Transonic Facility (NTF). The model was made of solid metal with cutouts under the wing along the span and additional cutouts in the outboard region for installation of measuring equipment. The wing geometry was designed and fabricated with a model jig twist distribution which will deform under load to the correct "1-G" twist at $M_\infty = 0.85$ and $C_L = 0.60$ [11]. The wing was equipped with 216 surface pressure orifices. Transition disks were applied to the wing surface to trap the transition at $Re = 4.3 \times 10^6$.

The finite element model of this wing is composed of 5937 nodes, 6705 elements and 17508 degrees of freedom, as shown in Figure 1. Eight-node solid hexagon elements are used to model the wing structure. The model was generated carefully so that there is a sufficient number of elements through the thickness of the wing. In addition, the finite element nodes were carefully defined on the plane of wing sections to maintain the bending characteristics of the wing. Moreover, all cutouts on the wing and the separation between the wing and its tip control surface were included in the model.

Calculations are performed for cruise and under-cruise conditions for $M_\infty = 0.85$ and $Re = 4.3 \times 10^6$ based on the mean aerodynamic chord. The pressure distributions are computed by the parallel version of the OVERFLOW code [2] on IBM SP-2 with a C-O type field grid containing $321 \times 81 \times 49$ grid points. The grid system of this wing was partitioned into five blocks to facilitate the distributed processing on IBM SP-2. The grid perturbation code, CSCMDO, was used to generate the deformed grid for every iteration.

For the cruise condition with $\alpha = 1.725^\circ$, Figure 2 shows the undeformed and deformed wing geometry based on the aerodynamic model. Figure 3 shows the pressure distributions at seven different spanwise locations for both the undeformed and deformed wings with circular symbols denoting the experimental data. As can be seen, the shock location moves forward and the suction peak changes drastically in the outboard region as the wing deforms. The predicted pressure distributions on the deformed wing are in good agreement with the experimental data. Also, the shock location and strength are captured well in the numerical solutions. The good agreement with data demonstrates that the present aero-structure interface method functions well, giving accurate results. The calculated results also indicate the significance of the aeroelastic effects.

Figure 4 shows similar results to those in Figure 3 for under-cruise conditions with $\alpha = 1.113^\circ$. Results again show that the predicted pressure distributions on the deformed wing are in good agreement with the experimental data and the aeroelastic effects are important.

4.0 MD-90 WING/FUSELAGE CONFIGURATION AT CRUISE CONDITIONS

We now apply the interface method to a wing/fuselage geometry and we choose the MD-90 configuration for this purpose. The original structural model of this configuration contains a wing box and a fuselage barrel near the wing root area. The fuselage barrel was extended to include the cockpit and tail sections by adding a series of beam elements with proper bending and torsion stiffness at the center of fuselage. In order to convert loads from the aerodynamic model to the structural model, dummy membrane elements (with zero stiffness and mass) were used to model the fuselage surface. The loads on the membrane elements are transformed to the center beam elements through rigid elements which form a wagon wheel shape at each fuselage cross section as shown in Figure 5. The skin, ribs and spars in the wing box were modeled by membrane elements and stringers by beam and rod elements. Additional dummy membrane elements were added to the leading and trailing edges of the wing in order to properly convert loads from the aerodynamic model into the finite element model. The finite element model contains 5,748 nodes, 14,518 elements and 32,931 degrees of freedom. Two points on the plane of symmetry of the wing/fuselage configuration are fixed to allow the bending deformation of the fuselage.

The pressure distributions on the surface of the MD-90 wing/fuselage at the cruise conditions with $M_\infty = 0.76$ and $\alpha = 2^\circ$ were computed by the OVERFLOW code with the Baldwin-Barth turbulence model. The parallel version of the OVERFLOW code on IBM SP-2 was used with the grid system of the MD-90 wing-fuselage partitioned into four blocks to facilitate the distributed processing. The C-O type field grid contained $289 \times 73 \times 49$ grid points with 225×49 grid points on the wing surface and 267×25 grid points on the fuselage surface. The grid perturbation technique was used to reduce work for grid generation at every iteration.

Figure 6(a) shows the deformed and undeformed wing/fuselage geometry of the aerodynamic model, and Figure 6(b) shows similar results for the wing model only, in which the fuselage is excluded. In the latter case, the root section of the wing is fixed. Therefore, the deflection at the wing tip is smaller. The smoothness of the geometry in Figure 6 demonstrates that our aero-structure interface procedure is functioning well for both wing and wing/fuselage configurations.

Figure 7 shows the pressure contours on the wing surface of the wing/fuselage configuration, and Figure 8 shows the pressure distributions at eight different spanwise locations for both deformed and undeformed wing/fuselage configurations as well as those for the wing-alone model. As can be seen, the aerodynamic pressures near the wing root remain almost the same and the shock location only changes slightly near the root.

However, the shock location moves toward the leading edge and the suction peak becomes smaller in the outboard region as the wing deforms.

The calculations show that near the leading edge there is a dip in the pressure coefficient on both the upper and lower surfaces of the wing when the wing/fuselage configuration deforms. However, this behavior is not observed in the wing-alone model. After a careful study, it is found that the dip in the pressure distribution is due to the separation between the slat and the wing box. In the wing-alone finite element model, the slat and the wing box are strongly connected to each other and the separation between them is not noticeable. However, in the finite element model of the wing/fuselage configuration, they are allowed to separate in order to simulate the real situation and the separation is a result of the structural deformation.

5.0 TRIM ANALYSIS

In aircraft trim analysis, the angle of attack and deflection of control surfaces are determined by balancing the aircraft payload by lift and pitching moment. In production design, the analysis is performed with a simplified structural finite element model and a linear aerodynamic code. The nonlinear aerodynamic effects are approximated by introducing correction factors to the aerodynamic influence coefficient (AIC) matrices. These factors are determined by wind tunnel test data. Although this approach is simple and computationally efficient, it relies on the wind tunnel test data and cannot accurately predict the nonlinear aerodynamic effects due to, for example, shock location changes with respect to the variation of angle of attack. Therefore, an accurate trim analysis method using detailed finite element models and advanced aerodynamic codes is desirable to improve the current production design approach.

In the present study, the angle of attack was considered to be the only trim variable. Two approaches, linear and nonlinear, were used to perform the trim analysis. The linear approach is based on linear aerodynamics, i.e., the aerodynamic loads (including force and pressure distribution) vary linearly with the angle of attack and elastic displacements. The deformed shape of the wing is represented by a linear combination of structural vibrational mode shapes. The trim angle and modal amplitudes are determined by solving the aeroelastic equations with a specified payload. This approach is simple and efficient but is limited to small angles of attack where nonlinear aerodynamic effects are not significant.

The nonlinear approach takes into account the nonlinearity of aerodynamics into the trim analysis. It directly searches for the trim angle with loads computed for the deformed shape of the aircraft by advanced aerodynamic codes. The aero-structure interface procedure is used to compute the deformed shape of the aircraft. Calculations are repeated several times to search for the trim angle for a specified payload. This approach gives accurate results at high angles of attack but is rather time-consuming when a large number of cases with different specified payloads are analyzed.

5.1 Linear Approach

In the linear approach, the aerodynamic loads are assumed to vary linearly with angle of attack and elastic displacements. The deformed shape of the wing is represented by a linear combination of structural vibration mode shapes. The aeroelastic equation is written as

$$K\mathbf{u} = \mathbf{F} \quad (11)$$

where K is the finite element stiffness matrix and \mathbf{u} the defection. The deflection can be expressed as the superposition of modal shapes as

$$\mathbf{u} = \phi_e \mathbf{c} \quad (12)$$

where ϕ_e is the matrix of modal shapes and \mathbf{c} is the generalized displacement vector containing the modal amplitudes. Based on the linear aerodynamics assumption, the aerodynamic forces \mathbf{F} on the wing can be written as

$$\mathbf{F} = \mathbf{F}_0 + \left[\frac{\partial \mathbf{F}}{\partial \mathbf{c}} \right] \mathbf{c} + \left\{ \frac{\partial \mathbf{F}}{\partial \alpha} \right\} \alpha \quad (13)$$

where \mathbf{F}_0 is the aerodynamic force on the undeformed wing at $\alpha = 0$.

From Eqs. (11)-(13), we get

$$K\phi_e \mathbf{c} = \mathbf{F}_0 + \left[\frac{\partial \mathbf{F}}{\partial \mathbf{c}} \right] \mathbf{c} + \left\{ \frac{\partial \mathbf{F}}{\partial \alpha} \right\} \alpha \quad (14)$$

Premultiplying Eq. (14) by ϕ_e^T , we obtain

$$K^* \mathbf{c} = \phi_e^T \mathbf{F}_0 + \phi_e^T \left[\frac{\partial \mathbf{F}}{\partial \mathbf{c}} \right] \mathbf{c} + \phi_e^T \left\{ \frac{\partial \mathbf{F}}{\partial \alpha} \right\} \alpha \quad (15)$$

where

$$K^* = \phi_e^T K \phi_e \quad (16)$$

The payload is balanced by the lift force so that

$$\phi_{plunge}^T \mathbf{F} = nW \quad (17)$$

where ϕ_{plunge}^T is the vector of the aircraft plunging motion, n is the load factor and W is the aircraft weight.

Substituting Eq. (13) into Eq. (17) results in

$$\phi_{plunge}^T \left(\underline{F}_0 + \left[\frac{\partial \underline{F}}{\partial \underline{c}} \right] \underline{c} + \left\{ \frac{\partial \underline{F}}{\partial \alpha} \right\} \alpha \right) = nW \quad (18)$$

Combining Eqs. (15) and (18) leads to the trim equation given below

$$\begin{bmatrix} K^* - \phi_e^T \left[\frac{\partial \underline{F}}{\partial \underline{c}} \right] & -\phi_e^T \left\{ \frac{\partial \underline{F}}{\partial \alpha} \right\} \\ \phi_{plunge}^T \left[\frac{\partial \underline{F}}{\partial \underline{c}} \right] & \phi_{plunge}^T \left\{ \frac{\partial \underline{F}}{\partial \alpha} \right\} \end{bmatrix} \begin{Bmatrix} \underline{c} \\ \alpha \end{Bmatrix} = \begin{Bmatrix} \phi_e^T \underline{F}_0 \\ nW - \phi_{plunge}^T \underline{F}_0 \end{Bmatrix} \quad (19)$$

The deflections and the angle of attack are then determined by solving Eq. (19).

The procedure for the linear approach can be summarized as follows:

- 1) Compute the aerodynamic loads on the undeformed wing at two different angles of attack and determine $\left\{ \frac{\partial \underline{F}}{\partial \alpha} \right\}$ using the finite difference approach.
- 2) Generate a set of structural vibration modal shapes with the finite element model.
- 3) At a specified angle of attack (usually zero degree) calculate the pressure distributions for a number of deformed wings by superposing each modal shape onto the undeformed wing geometry. $\left[\frac{\partial \underline{F}}{\partial \underline{c}} \right]$ is determined by the finite difference approach.
- 4) Solve the aeroelastic equations which balance the total lift with the specified payload in order to obtain the trim angle of attack and the modal amplitudes.
- 5) Obtain the deformed shape of the wing by superposing all modal shapes multiplied by the corresponding amplitudes on the undeformed wing. Also obtain the pressure distributions on the deformed wing by combining the pressure distributions corresponding to each modal shape and due to the angle of attack.

- 6) Calculate the pressure distributions on the deformed wing at the trim angle of attack using any advanced aerodynamic code and compare this with the pressure distributions obtained in step 5). The differences reflect the nonlinearity of the aerodynamic loads.

5.2 Nonlinear Approach

The procedure used in the nonlinear approach can be summarized as follows:

- 1) With an initial guess of the angle of attack, compute the aerodynamic loads on the undeformed aircraft.
- 2) Apply loads to the finite element model to compute deflection.
- 3) Obtain the deformed shape of the aircraft by superimposing the deflection on the undeformed aircraft geometry and recalculate the aerodynamic loads based on the deformed shape.
- 4) Repeat steps 2) to 3) to get converged solutions for both loads and deformations.
- 5) Calculate the lift of the deformed aircraft and compare it with the aircraft payload. If the payload is not balanced by lift, find a new angle of attack and repeat the calculations until the aircraft payload matches lift. Newton's method is used in the searching procedure to find the trim angle of attack.

5.3 Simple Wing at Transonic Conditions

A simple swept wing with a constant cross section of a NACA 0012 airfoil is used to conduct the linear and nonlinear trim analyses. The aspect ratio and sweep angle of the wing are 3.5 and 30°, respectively. This wing has been studied for transonic flow conditions with $M_\infty = 0.8$, $Re = 21 \times 10^6$. The pressure distribution on the surface of the wing is calculated with the OVERFLOW code for a C-O type field grid with $145 \times 29 \times 49$ grid points. The finite element model of the wing composed of membrane and rod elements is shown in Figure 9. The first eight structural vibration modal shapes shown in Figure 10 are used in the linear trim analysis.

Different payloads ranging from 10,000 pounds to 32,000 pounds are considered in the present study. Figure 11 shows the effect of the number of structural vibration modes used in the linear trim analysis and indicates that results based on four, six and eight vibration modal shapes are almost identical. This means that using only four vibration modes in the calculation is sufficient.

Table 1 presents the calculated trim angles of attack for different payloads for both linear and nonlinear approaches. It also includes the lift computed by the OVERFLOW code

with the trim angle of attack predicted by the linear approach. The difference between the payload and the lift represents the nonlinear effects of the aerodynamics. Figure 12 shows the lift predicted by both linear and nonlinear trim analysis as a function of the angle of attack. The dashed line, marked as "Linear Trim_CFD Analysis", is the lift calculated by the OVERFLOW code with the deformed geometry obtained from the linear trim analysis. It is found that the nonlinear aerodynamic effects become significant at higher angles of attack. It is also found that the lift calculated by "Linear Trim_CFD Analysis" is less than that by the nonlinear trim analysis.

Table 1. Trim angles of attack for different payloads

Payload	Trim Angle of Attack (Linear Approach)	Trim Angle of Attack (Nonlinear Approach)	Lift Predicted by OVERFLOW with Trim Angle Given by Linear Approach
10,000 lbs	2.164	2.158	10169 lbs
20,000 lbs	4.327	4.320	20140 lbs
25,000 lbs	5.409	5.463	24665 lbs
30,000 lbs	6.491	7.047	28268 lbs
32,000 lbs	6.923	8.017	28975 lbs

Figure 13 shows the pressure distributions at four spanwise locations for $\alpha = 2.158^\circ$ which corresponds to a payload of 10,000 pounds based on the nonlinear trim analysis. The pressure distribution predicted by the linear approach is denoted by the solid line and that predicted by the nonlinear approach by the dotted line. The dashed line, marked as "Linear Trim_CFD", represents the pressure distribution calculated by the OVERFLOW code with the deformed geometry obtained from the linear trim analysis. It is found that results from both the nonlinear trim analysis and the "Linear Trim_CFD" analysis agree well but the linear trim analysis fails to predict the pressure peak and the shock location accurately. It indicates that the nonlinear aerodynamic effect can not be neglected even at this low angle of attack.

Figure 14 shows similar results for $\alpha = 5.463^\circ$ which corresponds to a payload of 25,000 pounds based on the nonlinear trim analysis. Figure 15 shows results for $\alpha = 8.017^\circ$ which correspond to a payload of 32,000 pounds based on the nonlinear analysis. However, at such high angle of attack, the results based on the "Linear Trim_CFD" analysis deviate from those of the nonlinear approach. It is found that the pressure peak and the shock location in the outboard region cannot be predicted accurately by the "Linear Trim_CFD" analysis. The differences are caused by the inaccurate deformed geometry from the linear trim analysis.

6.0 HIGH-LIFT CONFIGURATIONS

As for wing and wing/fuselage configurations, the calculation of the aeroelastic effects of high-lift configurations requires the coupling of aerodynamics and structure. The latter is again analyzed by the same finite element code used for wing and wing/fuselage configurations. The calculation of aerodynamic loads may be based on two different approaches. The first one solves the Navier-Stokes equations directly, and the second makes use of the coupled solutions of the inviscid and viscous flow equations with an interaction law. This latter approach, sometimes referred to as the interactive boundary layer approach, solves the inviscid flow equations by a panel method and viscous flow equations by an inverse boundary layer method.

Regardless of which approach is used for aerodynamic calculations, it is necessary to calculate the onset of transition in each method. This requirement adds to the complexity of the calculations as well as leading to higher computational time. Furthermore, the optimization of the high-lift configuration will substantially increase the computational time. For these reasons, we have decided first to use the interactive boundary layer approach to calculate the aerodynamic loads of the high-lift configuration and perform the aerodynamic optimization. It should be pointed out that our interface method is general. Therefore, the aeroelastic effects of the high-lift configuration can be studied using the interactive boundary layer method as well as a Navier-Stokes code.

The configuration we choose to conduct our studies is the MD-90 high-lift configuration shown in Figures 16 and 17. Preliminary studies for a wing/fuselage configuration consisted of 1600 panels for the wing and around 5000 panels for the fuselage using the Douglas Neumann code indicated that the required computer time is around 100 minutes on a single node of IBM SP-2. An estimate for the computer time requirements with viscous effects included in the calculation using the interactive boundary layer approach will be around 400 minutes. To include the aeroelastic effects in the calculation will increase the computer time to 500 minutes for one iteration. If we assume, as for wing and wing/fuselage configurations, three iterations between aerodynamic and structural calculations are enough, the required computer time will be around 1500 minutes or 25 hours on a single node of IBM SP-2.

The above estimates do not include the aerodynamic optimization of the high-lift configuration which will undoubtedly increase the computer time substantially. It is clear that aeroelastic analysis of high-lift configurations must take advantage of the parallel processing of IBM SP-2 to reduce the computer time of 25 hours on a single node. For example, for 25 nodes, the computer time will be reduced to 1 hour and 100 nodes, it will be reduced to 15 minutes.

Current work will address the following tasks:

- (1) Repaneling for the MD-90 high-lift configuration
- (2) Parallelization of the Douglas Neumann code

- (3) Post processing of aerodynamic results on IBM SP-2
- (4) Testing the aerodynamic optimization procedure for two-dimensional high-lift configurations
- (5) Adaptation of the parallelized optimization procedure to Douglas Neumann code with assigned design variables
- (6) Finite-element modeling of the MD-90 high-lift configuration
- (7) Conducting aeroelastic analysis

7.0 AN IMPROVED CEBECI-SMITH TURBULENCE MODEL FOR BOUNDARY-LAYER AND NAVIER-STOKES METHODS

Today, most Navier-Stokes methods employ the Baldwin-Lomax turbulence model [5], which is a modified version of the Cebeci-Smith (CS) algebraic eddy-viscosity model developed for boundary-layer flows [4]. The main difference between the two models lies in the length scale used in the outer eddy viscosity. The Cebeci and Smith formulation uses the displacement thickness δ^* as the length scale; since δ^* is not well defined in the Navier-Stokes calculations due to the lack of precise definition of the boundary-layer thickness, Baldwin and Lomax use alternative expressions for the length scale. The studies conducted by Stock and Haase [6], however, clearly demonstrate that the modified algebraic eddy-viscosity formulation of Baldwin and Lomax is not a true representation of the CS model, since their incorporation of the length scale in the outer eddy viscosity is not appropriate for flows with strong pressure gradient.

Studies conducted with Navier-Stokes methods using the Baldwin-Lomax model confirm the studies of Stock and Haase [6] and indicate a need for a better model. The Cebeci-Smith model, on the other hand, while satisfactory at low to moderate pressure gradient flows, requires improvements for strong pressure gradient flows that are typical to flows either approaching stall or post-stall.

The main weakness in the CS model is the parameter α used in the outer eddy-viscosity formula, which in the original formulation was taken as 0.0168. Experiments indicate, however, that in strong pressure gradient flows, the extent of the law of the wall region becomes smaller; to predict flows under such conditions, it is necessary to have a smaller value of α in the outer eddy-viscosity formula. The question is how to relate α to the flow properties so that the influence of adverse pressure gradient is included in the variation of α .

In this section we discuss an improved CS model for boundary-layer and Navier-Stokes methods and present results obtained with this model as well as with other models based on the original CS model. In the following subsection we first present a brief description of the original CS model and its modified versions in order to adopt this model into

Navier-Stokes methods. This subsection is followed by a discussion and review of the improvements proposed to the CS model, either for boundary-layer methods or Navier-Stokes methods. Calculated results obtained with the interactive boundary-layer method of Cebeci [9] as well as with the Navier-Stokes method of Swanson and Turkel [12] are presented in subsections 7.3 and 7.4.

7.1 Original CS Model and Its Modified Versions

The Cebeci-Smith model treats a turbulent boundary-layer as a composite layer with inner and outer regions. In the inner region of a smooth surface without mass transfer, the eddy viscosity $(\varepsilon_m)_i$ is written as

$$(\varepsilon_m)_i = \ell^2 \left| \frac{\partial u}{\partial y} \right| \gamma_{tr}, 0 \leq y \leq y_c \quad (20)$$

Here the mixing length ℓ is given by

$$\ell = \kappa y \left[1 - \exp\left(-\frac{y}{A}\right) \right] \quad (21a)$$

where $\kappa = 0.40$ and A is a damping-length constant represented by

$$A = 26 \nu u_\tau^{-1}, u_\tau = \left(\frac{\tau}{\rho} \right)_{\max}^{1/2}, \quad \frac{\tau}{\rho} = (\nu + \varepsilon_m) \frac{\partial u}{\partial y} \quad (21b)$$

In Eq. (20) γ_{tr} is an intermittency factor which represents the streamwise region from the onset of transition to turbulent flow. It is given by

$$\gamma_{tr} = 1 - \exp \left[-G(x - x_{tr}) \int_{x_{tr}}^x \frac{dx}{u_e} \right] \quad (22)$$

where x_{tr} is the location of the onset of transition; factor G has the dimensions of *velocity/(length)* and is evaluated at the transition location by

$$G = \frac{3}{C^2} \frac{u_e^3}{\nu^2} R_{x_{tr}}^{-1.34} \quad (23)$$

where the transition Reynolds number R_{x_r} is $(u_e x / \nu)_{tr}$ and C is a constant with a recommended value of 60.

In the outer region, the eddy viscosity is given by

$$(\varepsilon_m)_o = \alpha u_e \delta^* \gamma_{tr} \gamma_c \leq y \leq \delta \quad (24)$$

Here γ is the intermittency factor for the outer region. With y_o defined as the y location where $u/u_e = 0.995$, it is given by

$$\gamma = \left[1 + 5.5 \left(\frac{y}{y_o} \right)^6 \right]^{-1} \quad (25)$$

based on Klebanoff's measurements on a flat plate flow. Continuity of the expressions for the eddy viscosities in the inner and outer regions, Eqs. (20) and (24), defines the boundaries of inner and outer regions. The parameter α in Eq. (24) is equal to 0.0168. Due to its simplicity and its good success in external boundary-layer flows, this model with modifications has also been used extensively in the solution of the Reynolds-averaged Navier-Stokes equations for turbulent flows. For the inner region, Baldwin and Lomax [5] use the expressions given by Eqs. (20) and (21). In the outer region, they use alternative expressions for the length scale δ^* of the form

$$(\varepsilon_m)_o = \alpha c_1 \gamma_{max} F_{max} \quad (26a)$$

or

$$(\varepsilon_m)_o = \alpha c_1 \gamma c_2 u_{diff}^2 \frac{y_{max}}{F_{max}} \quad (26b)$$

with $c_1 = 1.6$ and $c_2 = 0.25$. The quantities F_{max} and y_{max} are determined from the function

$$F = y \left(\frac{\partial u}{\partial y} \right) \left[1 - e^{-y/A} \right] \quad (27)$$

with F_{max} corresponding to the maximum value of F that occurs in a velocity profile and y_{max} denoting the y -location of F_{max} . u_{diff} is the difference between maximum and minimum velocity in the profile

$$u_{diff} = u_{max} - u_{min} \quad (28)$$

where u_{min} is taken to be zero except in wakes.

In Navier-Stokes calculations, Baldwin and Lomax replace the absolute value of the velocity gradient $\partial u/\partial y$ in Eqs. (20) and (27) by the absolute value of the vorticity $|\omega|$,

$$|\omega| = \left| \frac{\partial u}{\partial y} - \frac{\partial v}{\partial x} \right| \quad (29a)$$

and the intermittency factor γ in Eq. (25) is written as

$$\gamma = \left[1 + 5.5 \left(\frac{c_3 y}{y_{\max}} \right)^6 \right]^{-1} \quad (29b)$$

with $c_3 = 0.3$. The studies conducted by Stock and Haase [6] clearly demonstrate that the modified algebraic eddy viscosity formulation of Baldwin and Lomax is not a true representation of the CS model since their incorporation of the length scale in the outer eddy viscosity formula is not appropriate for flows with strong pressure gradients.

Stock and Haase proposed a length scale based on the properties of the mean velocity profile calculated by a Navier-Stokes method. They recommend computing the boundary-layer thickness δ from

$$\delta = 1.936 y_{\max} \quad (30)$$

where y_{\max} is the distance from the wall for which $y|\partial u/\partial y|$ or F in Eq. (27) has its maximum. With δ known, u_e in the outer eddy viscosity formula, Eq. (24), is the u at $y = \delta$, and γ is computed from Eq. (25) and not from Eq. (29b). The displacement thickness δ^* for attached flows is computed from its definition,

$$\delta^* = \int_0^\delta \left(1 - \frac{u}{u_e} \right) dy \quad (31a)$$

and, for separated flows from

$$\delta^* = \int_{y_{u=0}}^\delta \left(1 - \frac{u}{u_e} \right) dy \quad (31b)$$

either integrating the velocity profile from $y = 0$, or $y = y_{u=0}$, to δ , or using the Coles velocity profile. The results obtained with this modification to the length scale in the outer CS eddy viscosity formula improve the predictions of the CS model in Navier-Stokes methods as discussed in Stock and Haase [6].

A proposal which led to Eq. (30) was also made by Johnson [7]. He recommended that the boundary-layer thickness δ is calculated from

$$\delta = 1.2y_{1/2} \quad (32)$$

where

$$y_{1/2} = y \quad \text{at} \quad \frac{F}{F_{\max}} = 0.5 \quad (33)$$

7.2 Improvements to the Original CS Model

Extensive studies, mostly employing boundary-layer equations, show that while many external turbulent flow problems can satisfactorily be calculated with the original Cebeci-Smith eddy-viscosity formulation, improvements are needed for flows which contain regions of strong pressure gradient and flow separation. One approach developed by Johnson and King [8] and Johnson and Coakley [13] is to adopt a nonequilibrium eddy-viscosity formulation ϵ_m in which the CS model serves as an equilibrium eddy viscosity $(\epsilon_m)_{eq}$ distribution. An ordinary differential equation (ODE), derived from the turbulence kinetic energy equation, is used to describe the streamwise development of the maximum Reynolds shear stress, $-\overline{u'v'}$, or $(-\overline{u'v'})_m$ for short, in conjunction with an assumed eddy-viscosity distribution which has $\sqrt{(-\overline{u'v'})_m}$ as its velocity scale. In the outer part of the boundary-layer, the eddy viscosity is treated as a free parameter that is adjusted to satisfy the ODE for the maximum Reynolds shear stress. More specifically, the nonequilibrium eddy-viscosity distribution is defined again by separate expressions in the inner and outer regions of the boundary-layer. In the inner region, $(\epsilon_m)_i$ is given by

$$(\epsilon_m)_i = (\epsilon_{mi})_1 (1 - \gamma_2) + (\epsilon_{mi})_{J-K} \gamma_2 \quad (34)$$

where $(\epsilon_{mi})_1$ is given either by $(\kappa y)^2 \partial u / \partial y$ or $u_\tau y$. The expression $(\epsilon_{mi})_{J-K}$ is

$$(\epsilon_{mi})_{J-K} = D^2 \kappa y u_m \quad (35)$$

where

$$u_m = \max \left(u_\tau, \sqrt{(-\overline{u'v'})_m} \right) \quad (36a)$$

and D is a damping factor similar to that defined by Eq. (21a),

$$D = 1 - \exp \left(\sqrt{(-\overline{u'v'})_m} \frac{y}{\nu A^+} \right) \quad (36b)$$

with the value of A^+ equal to 17 rather than 26, as in Eq. (21a). The parameter γ_2 in Eq. (34) is given by

$$\gamma_2 = \tanh \left(\frac{y}{L'_c} \right) \quad (36c)$$

where, with y_m corresponding to the y -location of maximum turbulent shear stress, $(-\overline{u'v'})_m$,

$$L'_c = \frac{u_\tau}{u_\tau + u_m} L_m \quad (37)$$

with

$$L_m = \begin{cases} 0.4 y_m y_m \leq 0.225\delta \\ 0.09\delta y_m > 0.225\delta \end{cases} \quad (38)$$

In the outer region, $(\varepsilon_m)_o$ is given by

$$(\varepsilon_m)_o = \sigma(0.0168 u_e \delta^* \gamma) \quad (39)$$

where σ is a parameter to be determined. The term multiplying σ on the right-hand side of Eq. (39) is the same as the expression given by Eq. (24) without γ_{fr} and with $\alpha = 0.0168$.

The nonequilibrium eddy viscosity across the whole boundary-layer is computed from

$$\varepsilon_m = (\varepsilon_m)_o \tanh \left[\frac{(\varepsilon_m)_i}{(\varepsilon_m)_o} \right] \quad (40)$$

The maximum Reynolds shear stress $(-\overline{u'v'})_m$ is computed from the turbulence kinetic energy equation using assumptions similar to those used by Bradshaw et al [14]. After the modeling of the diffusion, production and dissipation terms and the use of

$$\frac{(-\overline{u'v'})_m}{k_m} = a_1 = 0.25$$

the transport equation for $(-\overline{u'v'})_m$ with u_m now denoting the streamwise velocity at y_m , is written as

$$\frac{d}{dx} (-\overline{u'v'})_m = \frac{a_1 (-\overline{u'v'})_m}{L_m u_m} \left[(-\overline{u'v'})_{m,eq}^{\frac{1}{2}} - (-\overline{u'v'})_m^{\frac{1}{2}} \right] - \frac{a_1}{u_m} D_m \quad (41)$$

where, with $c_{dif} = 0.5$, the turbulent diffusion term along the path of maximum $(-\overline{u'v'})$ is given by

$$D_m = \frac{c_{dif}}{a_1 \delta} \frac{(-\overline{u'v'})_m^{\frac{3}{2}}}{[0.7 - (y/\delta)_m]} \left\{ 1 - \left[\frac{(-\overline{u'v'})_m}{(-\overline{u'v'})_{m,eq}} \right]^{\frac{1}{2}} \right\} \quad (42)$$

To use this closure model, the continuity and momentum equations are first solved with an equilibrium eddy viscosity $(\varepsilon_m)_{eq}$ distribution such as in the CS model, and the maximum Reynolds shear stress distribution is determined based on $(\varepsilon_m)_{eq}$, which we denote by $(\overline{u'v'})_{m,eq}$. Next the location of the maximum Reynolds shear stress is determined so that y_m and u_m can be calculated. The transport equation for $(\overline{u'v'})_m$ is then solved to calculate the nonequilibrium eddy-viscosity distribution ε_m given by Eq. (40) for an assumed value of σ so that the solutions of the continuity and momentum equations can be obtained. The new maximum shear stress term is then compared with the one obtained from the solution of Eq. (41). If the new computed value does not agree with the one from Eq. (41), a new value of σ is used to compute the outer eddy viscosity and eddy-viscosity distributions across the whole boundary-layer so that a new $(\overline{u'v'})_m$ can be computed from the solution of the continuity and momentum equations. This iterative procedure of determining σ is repeated until $(\overline{u'v'})_m$ is computed from the continuity and momentum equations agrees with that computed from the transport equation, Eq. (41).

Another approach to improve the predictions of the CS model flows with adverse pressure gradient and separation is to relate the parameter α to a parameter F , according to the suggestion of Simpson, et al. [15], by

$$\alpha = \frac{0.0168}{F^{1.5}} \quad (43)$$

Here $(1 - F)$ denotes the ratio of the production of the turbulence energy by normal stresses to that by shear stress, evaluated at the location where shear stress is maximum, that is

$$F = 1 - \left[\frac{(\overline{u'^2} - \overline{v'^2}) \partial u / \partial x}{-\overline{u'v'} \partial u / \partial y} \right] \quad (44)$$

Before Eq. (43) can be used in Eq. (24), an additional relationship between $(\overline{u'^2} - \overline{v'^2})$ and $(-\overline{u'v'})$ is needed. For this purpose, the ratio in Eq. (44)

$$\beta = \left[\frac{\overline{u'^2} - \overline{v'^2}}{-\overline{u'v'}} \right] \quad (45)$$

is assumed to be a function of $Re = \tau_w / (\rho \overline{u'v'})_m$ which, according to the data of Nakayama, [16] can be represented by

$$\beta = \frac{6}{1 + 2R_t(2 - R_t)} \quad (46a)$$

for $R_t < 1.0$. For $R_t \geq 1.0$, β is taken to be

$$\beta = \frac{2R_t}{1 + R_t} \quad (46b)$$

Introducing the above relationships into the definition of F and using Eq. (40) results in the following expression for α

$$\alpha = \frac{0.0168}{[1 - \beta(\partial u / \partial x) / (\partial u / \partial y)]^{1.5}} \quad (47)$$

where β is given by Eq. (46).

Another improvement to the CS model can be made by replacing the intermittency parameter γ in Eq. (25) by another intermittency expression recommended by Fiedler and Head [17]. According to the experiments conducted by Fiedler and Head it was found that the pressure gradient has a marked effect on the distribution of intermittency defined as the ratio of time turbulent to total time at any point so that it measures the probability of finding turbulent flow at any instant at the point considered. Their experiments indicated that in the boundary-layer proceeding to separation, the intermittent zone decreases in width and moved further from the surface as shape factor H increases. The reverse trend is observed with decreasing H in a favorable pressure gradient.

In the improved CS model the intermittency expression of Fiedler and Head is written in the form

$$\gamma = \frac{1}{2} \left[1 - \operatorname{erf} \frac{[y - Y]}{\sqrt{2}\sigma} \right] \quad (48)$$

where Y and σ are general intermittency parameters with Y denoting value of y for which $\gamma = 0.5$ and σ , the standard deviation. The dimensionless intermittency parameters Y/δ^* and σ/δ^* expressed as functions of H are shown in Fig. 18.

7.3 Predictions of the Original and Improved CS Model by the Cebeci Interactive Boundary-Layer Method

The predictions of the original and modified Cebeci-Smith turbulence models were investigated for several airfoils by using interactive boundary-layer and Navier-Stokes methods. For each airfoil, the onset of the transition location was computed with Michel's correlation [9] and the calculated lift coefficients were compared with data for a range of angles of attack, including stall and post stall.

A complete description and evaluation of the interactive boundary-layer (IBL) method used here is presented in Cebeci [9] for high and low Reynolds numbers at low Mach numbers and for a wide range of angles of attack. This method employs an inverse boundary-layer procedure in which the governing equations are solved for a compressible flow with the inviscid flow and viscous flow equations coupled with Veldman's interaction law. The inviscid flow is computed either with a panel method or a full potential method. In the former case, compressibility effects are introduced by using the Prandtl-Glauert correction.

Figures 19a to 19e show the results obtained with the original and modified CS models, the latter corresponding to the one in which α is computed according to Eq. (47) and the intermittency factor due to Fiedler and Head. The experimental data in Figures 19a to 19c were obtained by Carr et al.[18] and those in Figures 19d and 19e by Omar et al. [19]. In all cases the inviscid flow calculations were made by using the full potential method.

As can be seen, the calculated results obtained with the modified CS model are significantly better than those obtained with the original CS model. In almost all cases, the calculated lift coefficients with the original CS model are much higher than those measured ones; in one case, Fig. 19d, the $(C_l)_{max}$ is not predicted at all. The modified CS model, on the other hand, in most cases, predicts the $(C_l)_{max}$ and produces lift coefficients for post stall which are in agreement with the trend of measured values.

Figures 20a to 20e show a comparison between the calculations and experimental results in which the calculated ones were obtained by using the modified CS and Johnson-King (JK) models. Overall, the predictions of the modified CS model are better than the JK model. For example, for the NACA 0012 airfoil, Fig. 20a, the modified CS model predicts $(C_l)_{max}$ more accurately than the JK model. For the Wortmann airfoil, Fig. 20b, the JK model does not predict the post-stall behavior of the lift coefficient. For the Ames airfoil, Fig. 20c, the predictions of both models are satisfactory with those obtained with the JK model are slightly better near $(C_l)_{max}$ than those with the CS model. For Boeing airfoils, the predictions of the modified CS model are better than the JK model near stall and especially post stall regions.

7.4 Predictions with a Navier-Stokes Method

The predictions of the original and modified CS models were also investigated by using the Navier-Stokes method of Swanson and Turkel [12]. The models considered include the original CS model, BL model, modifications to the BL model and the JK model.

Figures 21a to 21e show the results obtained with the original CS and BL models. In the former case, the length scale δ^* in the outer eddy-viscosity formula was computed based

on the definition of the boundary-layer thickness δ given by Stock and Haase [6] and Johnson [7].

Figures 22a to 22e show similar comparisons with turbulence models corresponding to the original CS and modified CS models. In the latter case the boundary-layer thickness was computed from

$$\delta = 1.5y_{1/2} \quad (49a)$$

or from

$$\delta = y_m \quad (49b)$$

if $1.5 y_{1/2} > y_m$, with y_m corresponding to the location where streamwise velocity u is maximum. Figures 23a to 23e show results obtained with turbulence models based on modified CS and BL-JK models. In the latter case, the parameter α in the BL method was taken as a variable computed by the JK method.

A comparison of results presented in Figures 21 and 22 show that for the airfoil flows considered here, the results obtained with the original CS model (Fig. 21) with δ defined by Stock and Haase [6] and Johnson [7] are slightly better than those given by the BL model and the results with the modified CS model (Fig. 22) are much better than all the other modified versions of the original CS model.

A comparison of the results obtained with the modified CS model and with the BL-JK model (Fig.23) show that both models essentially produce similar results.

Finally, Fig. 24 shows a comparison between the predictions of the IBL and NS methods. In both methods, the turbulence model used is the modified CS model. The IBL calculations made use of the full potential method discussed by Cebeci [9]. As can be seen, the predictions of both methods are identical at low and moderate angles of attack. At higher angles, especially near stall and post stall, while there are some differences, both methods predict the stall angle well. The savings in computing cost provided by the IBL method, however, is considerably less than those provided by the Navier-Stokes method.

8.0 CONCLUSIONS AND RECOMMENDATIONS

A general interface method developed in the first phase of the present contract is used to study the aeroelastic effects on an advanced transport wing at cruise and under-cruise conditions. Calculated results show good agreement with experimental data and indicate that aeroelastic effects have a pronounced effect on the aerodynamic performance of this wing.

The interface method was then applied to a MD-90 wing/fuselage configuration at cruise conditions. The effect of including fuselage in the calculation is also investigated by performing calculations for the wing-alone configuration. The smoothness of the deformed geometry indicates that the interface method functions well for both wing and wing/fuselage configurations.

An aircraft trim analysis was conducted with advanced aerodynamic codes using both linear and nonlinear approaches. The former assumes a linear variation of aerodynamic loads and structural deformation with respect to modal amplitudes. On the contrary, the latter approach uses a coupling procedure between aerodynamic and structural models and searches for the trim angle of attack iteratively. The results indicate that while the linear approach is accurate at small angles of attack, it becomes less accurate at higher angles of attack where the nonlinear effects are more pronounced. As a result, it is necessary to conduct the trim analysis with the nonlinear approach to get accurate results.

The accuracy of turbulence models based on the algebraic eddy viscosity formulation of Cebeci and Smith is studied for airfoil flows at low Mach numbers. Studies conducted by interactive and Navier-Stokes methods using several versions of this model show that recently developed version of this model due to Cebeci and Chang produce results significantly better than those obtained with the original CS model. Studies are in progress to extend the improved CS model to three-dimensional flows.

The next phase of the studies will concentrate on the calculation of the aeroelastic effects of high lift configurations. Initially the aero portion of the calculations will utilize a panel method with boundary layer corrections. Since the interface method is a general one, however, once the procedure of coupling the aero with the finite element is completed, the same procedure can also be used for calculations in which aero portion of the calculations will utilize a Navier-Stokes method.

References

1. Tzong, T., Chen, H. H., Chang, K. C., Wu, T. And Cebeci, T., "A General Interface Method for Aeroelastic Analysis of Aircraft," McDonnell Douglas Report No. MDC 96K7062, Feb. 1996.
2. Buning, P. G., Jespersen, D. C., Pulliam, T. H., Chan, W. M., Slotnick, J. P., Krist, S. E. and Renze, K., J., "OVERFLOW User's Manual, Version 1.7r," NASA Ames Research Center, Moffett Field, CA, 1996.
3. Hess, J. L., Friedman, D. M., and Clark, R. W., "Calculation of Compressible Flow About Three-Dimensional Inlets with Auxiliary Inlets, Slats and Vanes by Means of a Panel Method," NASA Contractor Report 174975, 1985.
4. Cebeci, T. and Smith, A.M.O., *Analysis of Turbulent Boundary-Layers*, Academic Press, NY, 1974.
5. Baldwin, B.S. and Lomax, H., "Thin Layer Approximation of Algebraic Model for Separated Turbulent Flows," AIAA paper No. 78-257, Jan. 1978.
6. Stock, H.W. and Haase, W., "Determination of Length Scales in Algebraic Turbulence Models for Navier-Stokes Methods," *AIAA J.*, Vol. 27, No.1, pp. 5-14, 1989.
7. Johnson, D.A., "Nonequilibrium Algebraic Turbulence Modeling Considerations for Transonic Airfoils and Wings," AIAA paper No. 92-0026, Jan. 1992.
8. Johnson, D.A. and King, L.S., "Mathematically Simple Turbulence Closure Model for Attached and Separated Turbulent Boundary Layers," *AIAA J.*, Vol. 23, No. 11, pp. 1684-1692, 1985.
9. Cebeci, T., *An Engineering Approach to the Calculation of Aerodynamic Flows*, to be published, 1997.
10. Jones, W. T. and Samareh-Abolhassani, J., "A Grid Generation System for Multi-Disiplinary Design Optimization," AIAA CP 95-1689, 1995.
11. Wilcox, P. A., "Operating Report for the Wind Tunnel Test of the 2.426% Scale M=0.85 Advanced Transport Model, LB-559D, in the NASA Langley Research Center National Transonic Facility (NTF)," McDonnell Douglas Report No. MDC 96K0203, Feb. 1996.
12. Swanson, R.C., Turkel, E., "A Multistage Time-Stepping Scheme for the Navier-Stokes Equations," AIAA paper No. 85-0035, Jan. 1985.
13. Johnson, D.A. and Coakley, T.J., "Improvement to a Nonequilibrium Algebraic Turbulence Model," *AIAA J.*, Vol. 28, No. 11, pp. 2000-2003, 1990.
14. Bradshaw, P., Ferriss, D.H. and Atwell, N.P., "Calculation of Boundary-Layer Development Using the Turbulent Energy Equation," *J. Fluid Mech.*, Vol. 18, p. 593, 1967.
15. Simpson, R.L., Chew, Y.T. and Shivaprasad, B.G., "The Structure of a Separating Turbulent Boundary Layer, Part 1, Mean Flow and Reynolds Stresses," *J. Fluid Mech.*, Vol. 113, pp. 23-51, 1981.
16. Nakayama, A., "Measurements in the Boundary Layer and Wake of Two Airfoil Models," Report No. MDC J2403, Douglas Aircraft Co., June 1982.

17. Fiedler, H. and Head, M.R., "Intermittency Measurements in the Turbulent Boundary Layer," *J. Fluid Mech.*, Vol. 25, Part 4, pp. 719-735, 1966.
18. Carr, L.W., McCroskey, W.J., McAlister, K.W., Pucci, S.L. and Lambert, O., *An Experimental Study of Dynamic Stall on Advanced Airfoil Sections, Vol. 3, Hot-Wire and Hot-Film Measurements*, NASA TM 84245.
19. Omar, E., Zierten, T., Hahn, M., Szpiro, E. and Mahal, A., *Two-Dimensional Wind-Tunnel Tests of a NASA Supercritical Airfoil with Various High-Lift Systems, Vol. 2, Test Data*, NASA CR-2215, 1977.

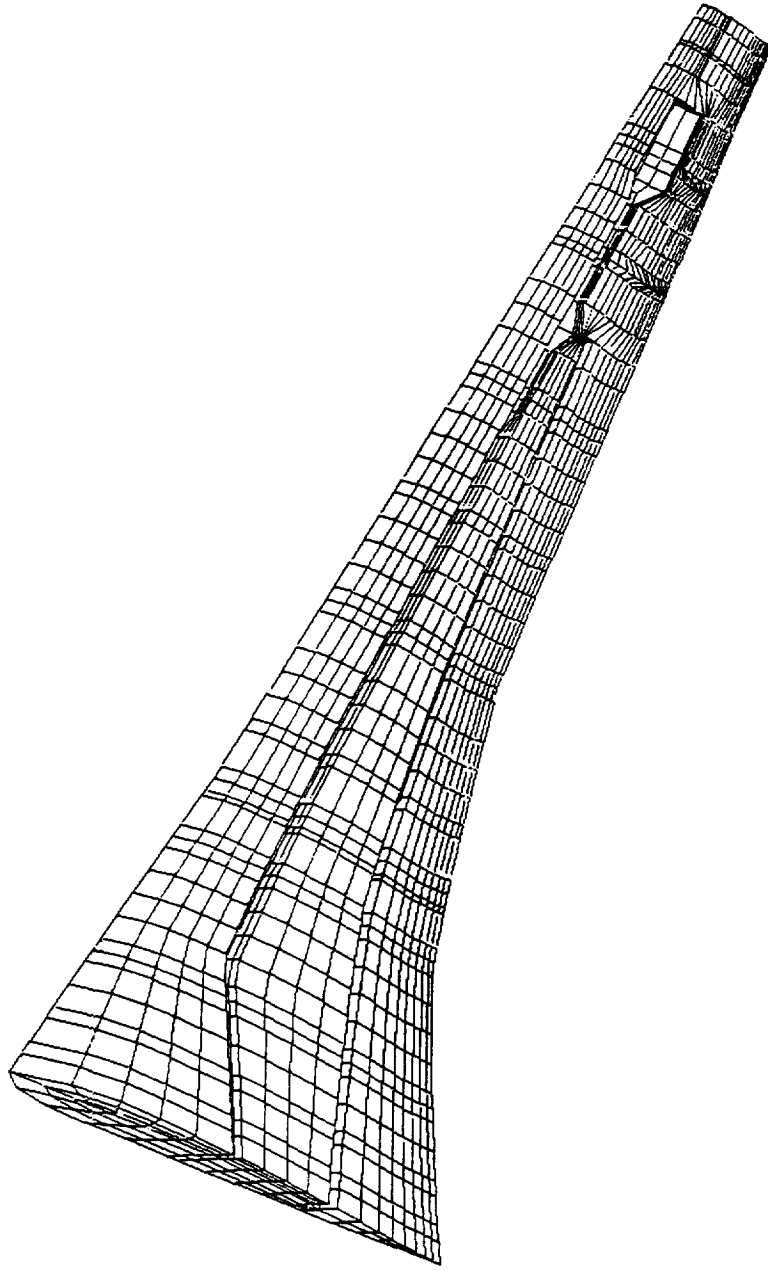


Fig. 1 The finite element model of the advanced transport wing

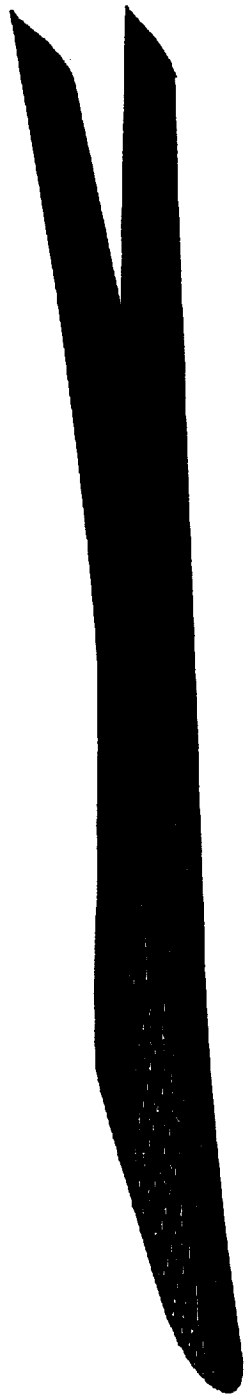


Fig. 2 The undeformed and deformed geometry of the advanced transport wing at the cruise condition

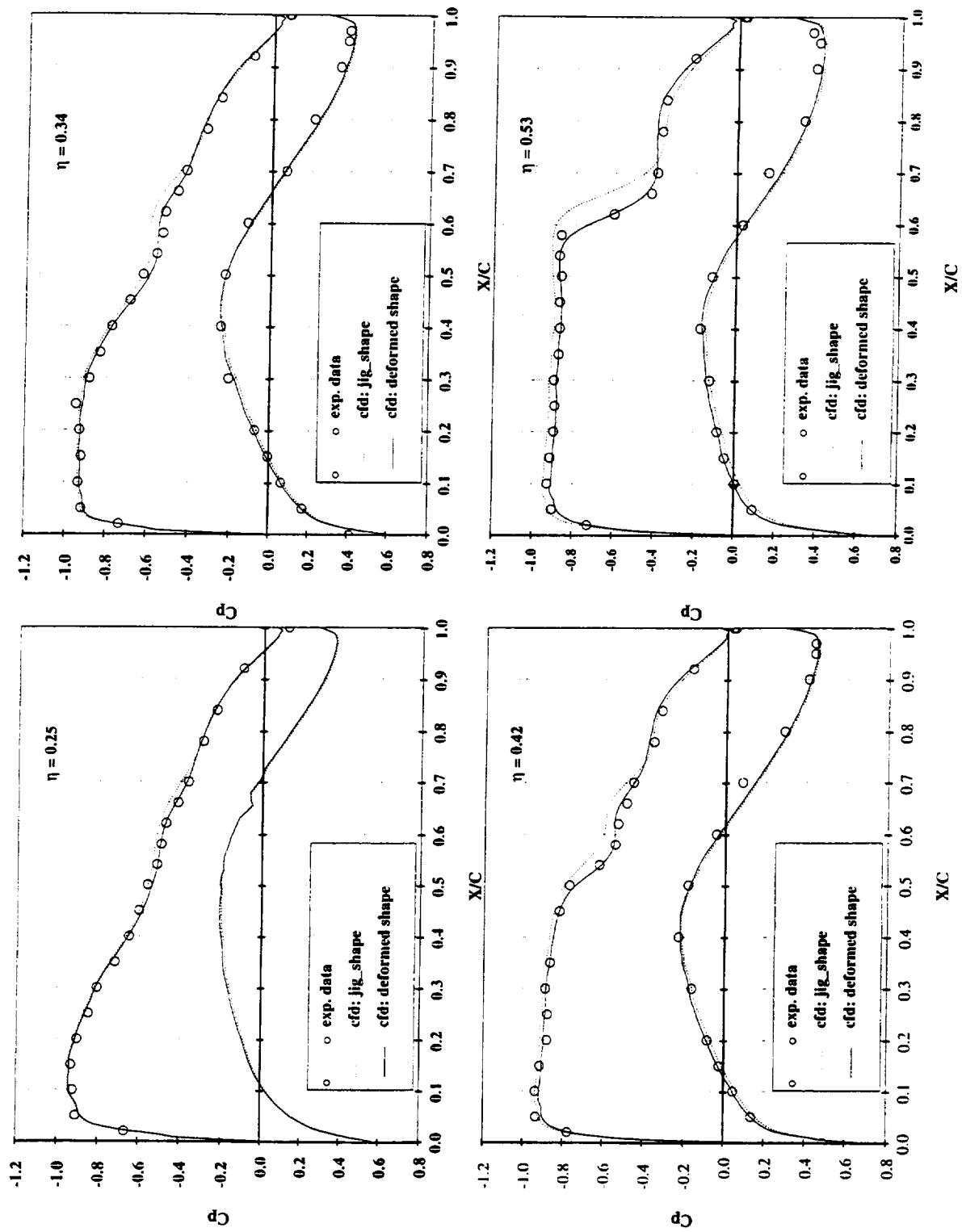


Figure 3. The pressure distributions at seven spanwise locations of the advanced transport wing at $\alpha = 1.725^\circ$

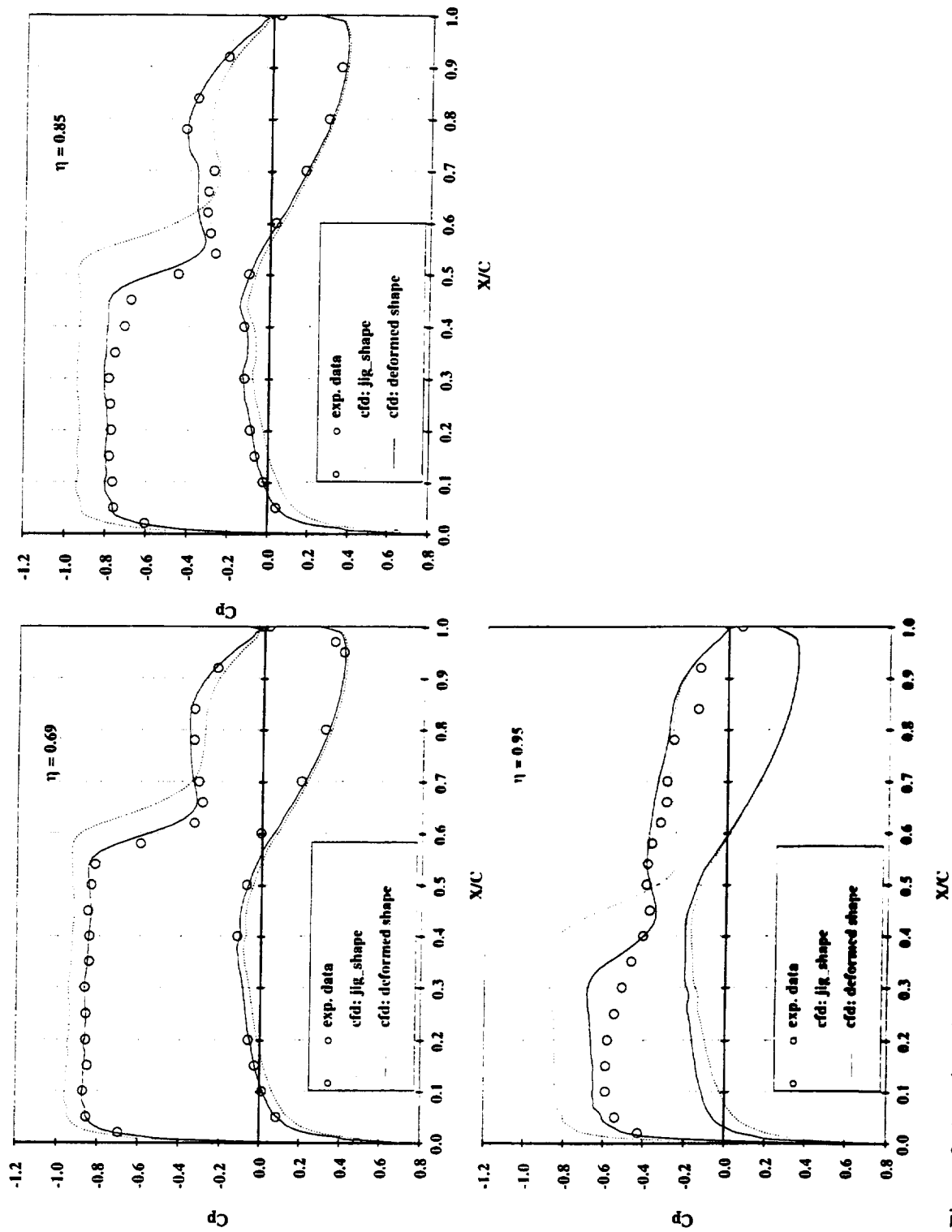


Figure 3. (continued)

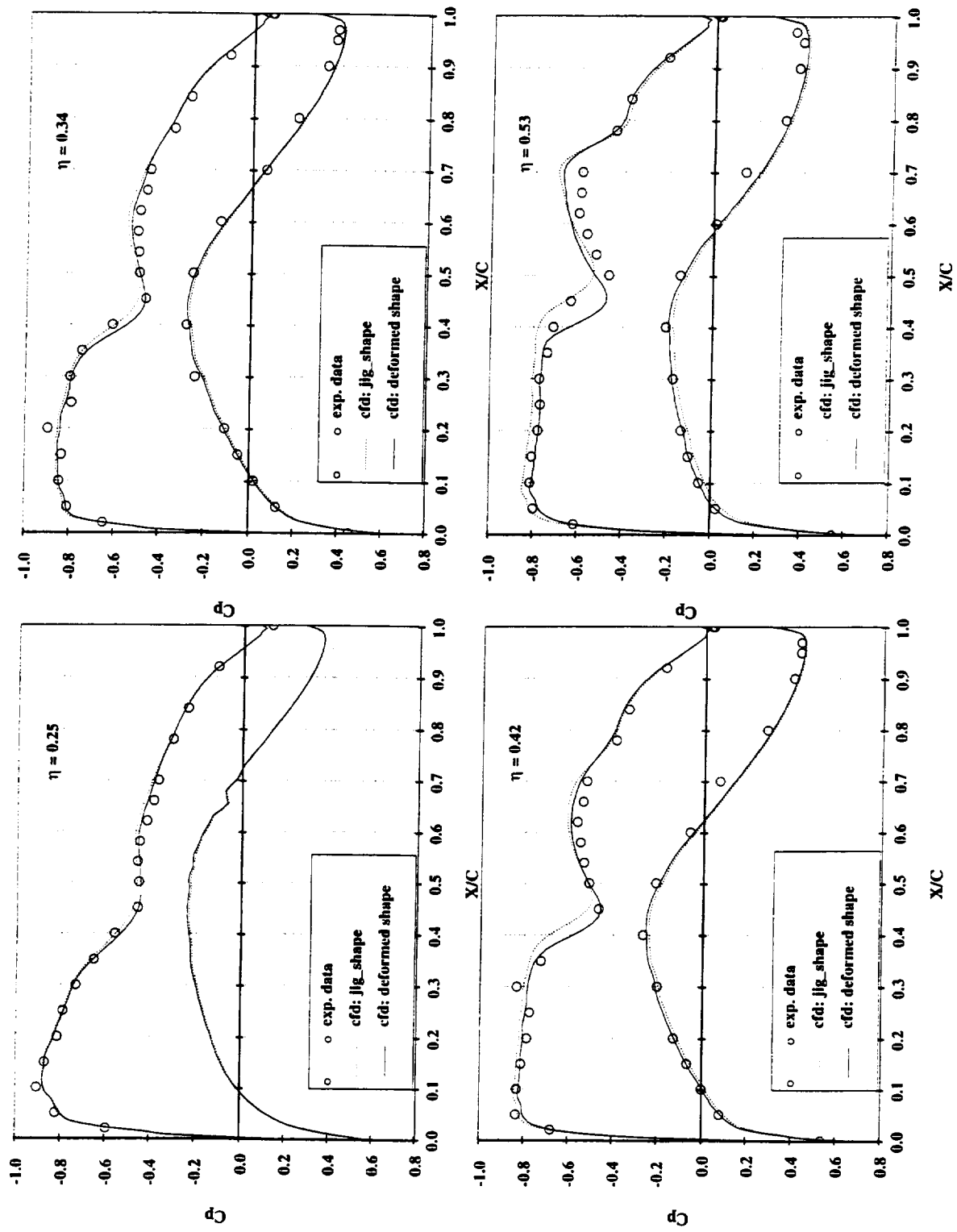


Figure 4. The pressure distributions at seven spanwise locations of the advanced port wing at $\alpha = 1.13^\circ$

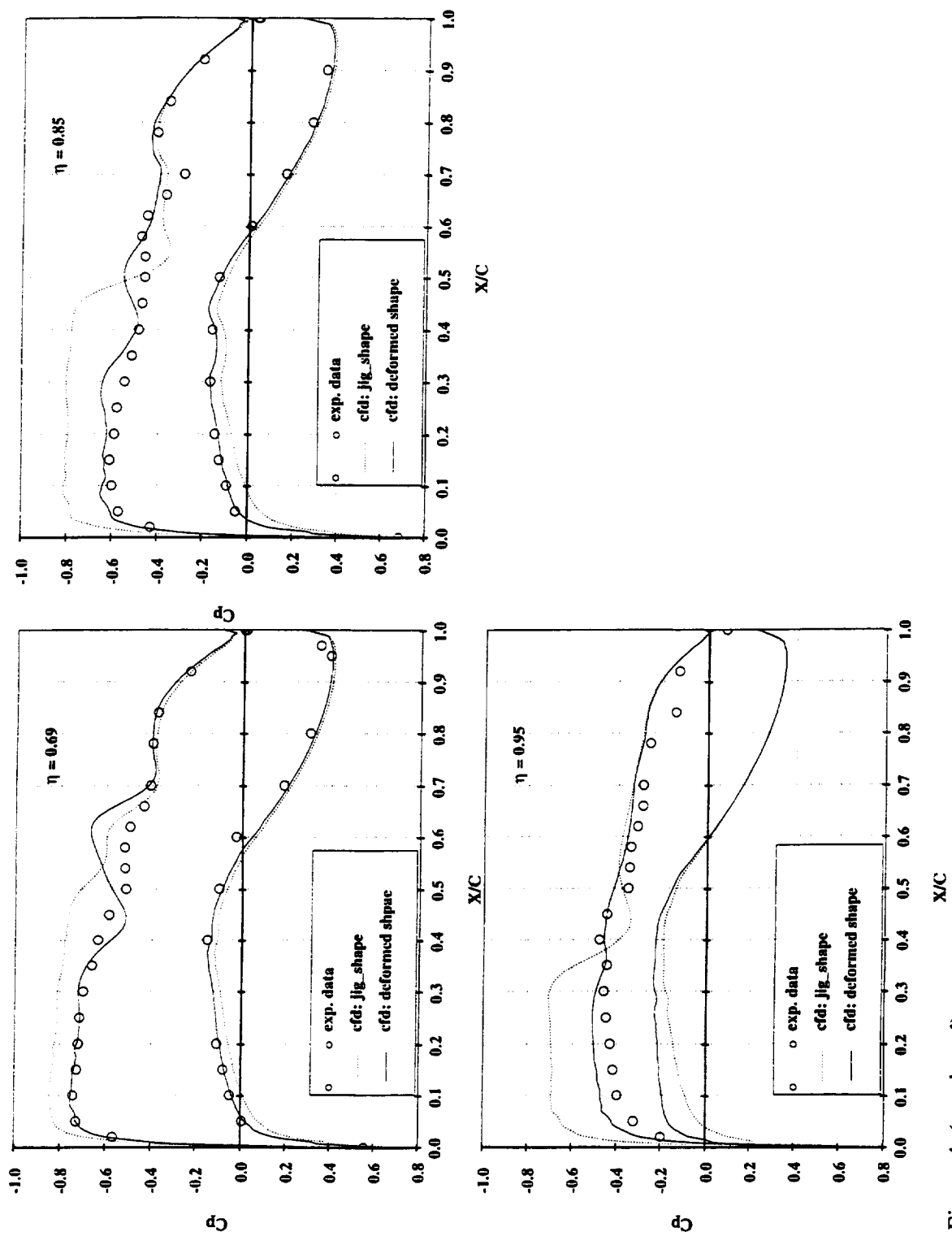
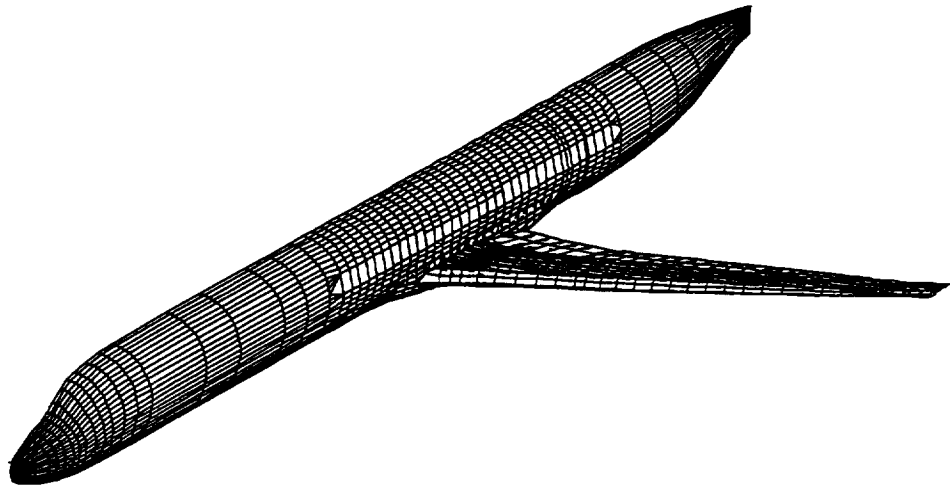


Figure 4. (continued)

View 1



View 2

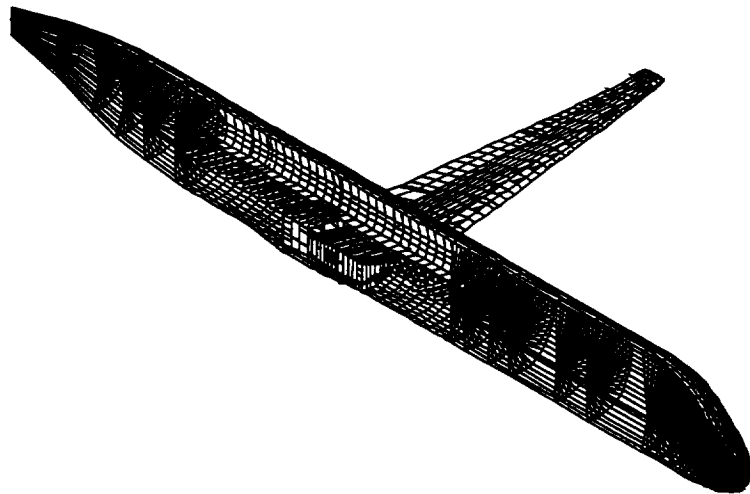


Fig. 5 The finite element model of the MD-90 wing/fuselage configuration

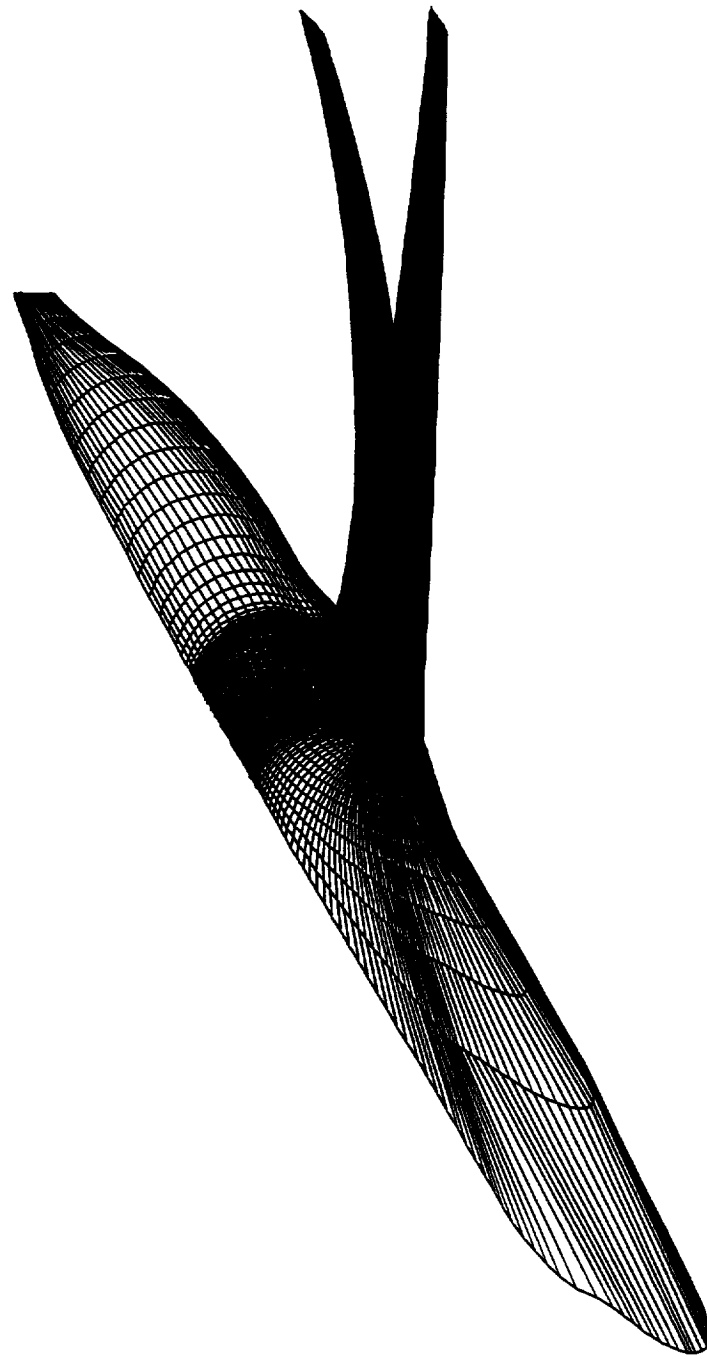


Fig. 6(a) The undeformed and deformed geometry of the MD-90 wing/fuselage configuration



Fig. 6(b) The undeformed and deformed geometry of the MD-90 wing

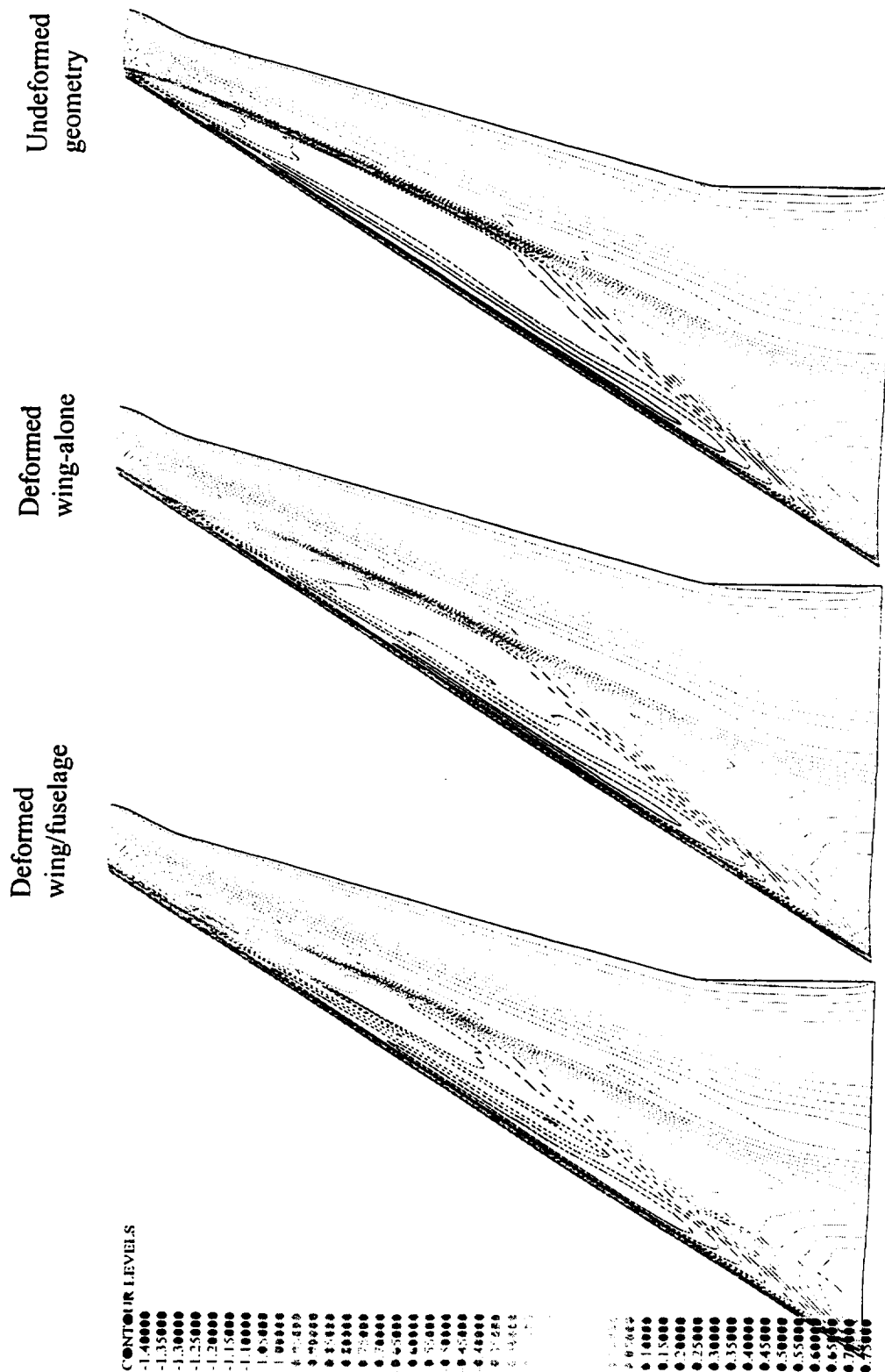


Fig. 7 The pressure contours on the undeformed and deformed MD-90 wing/fuselage

COMPARISON OF CHORDWISE PRESSURE DISTRIBUTIONS

Aeroelasticity Effect on MD90 Wing/Body

REN = 27.6 M, MACH = .760, ALPHA = 2.00

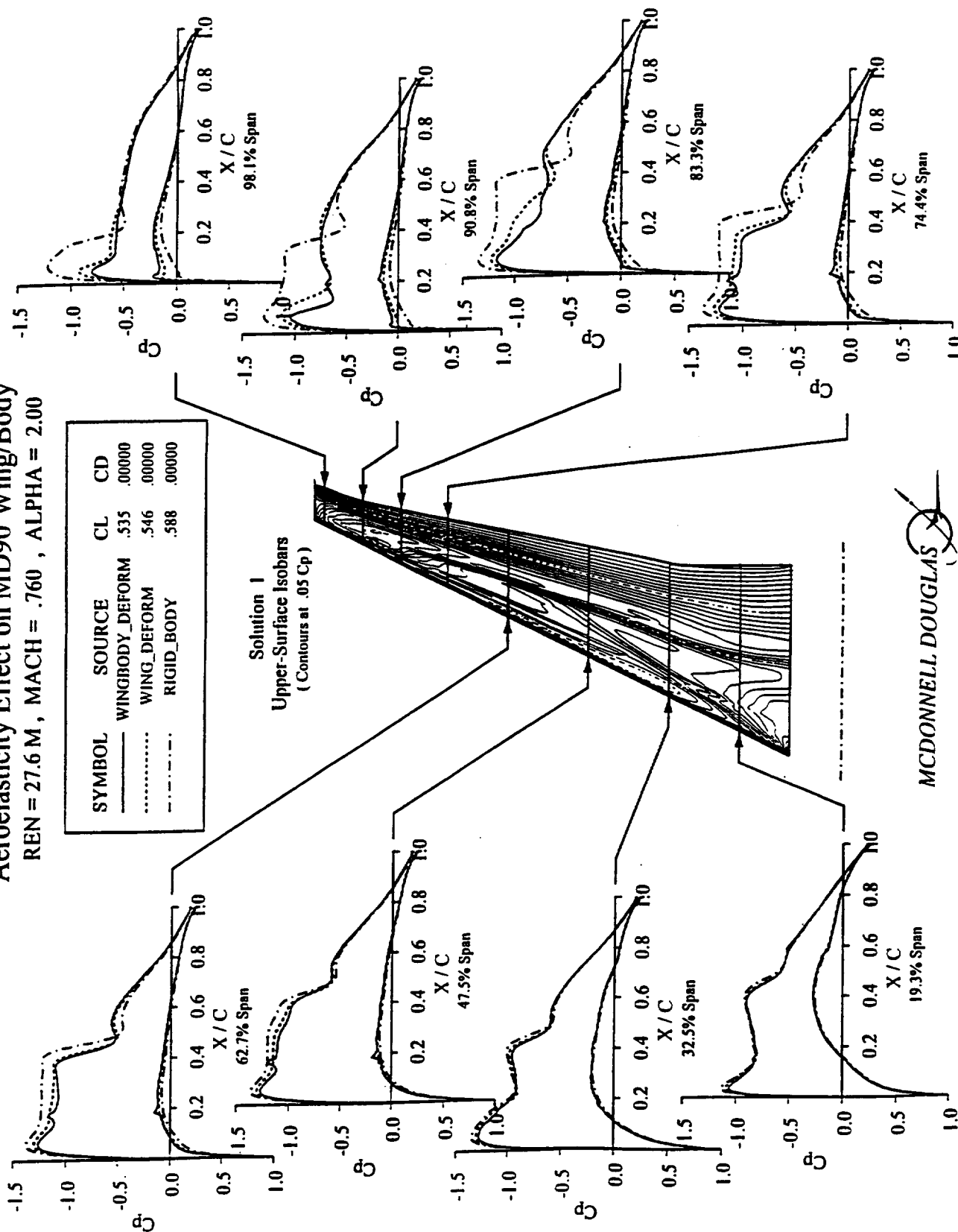


Figure 8 - The pressure distributions at eight spanwise locations of the MD-90 wing/fuselage configuration

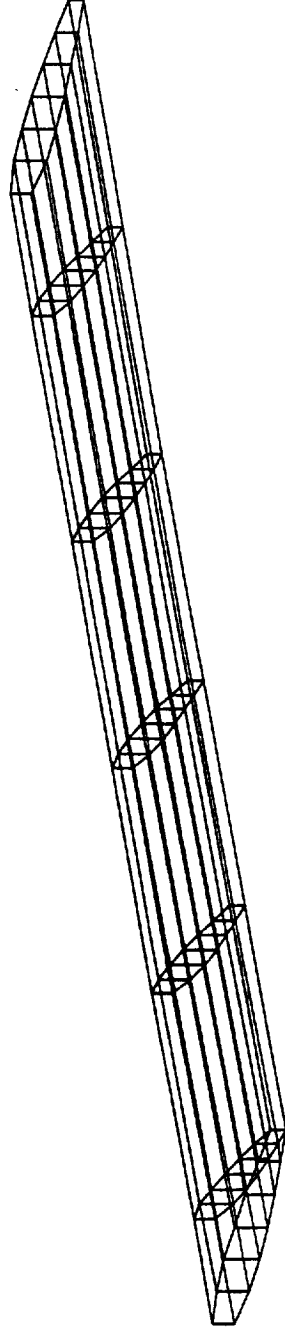


Figure 9. The finite element model of the simple wing

MODE 1



Fig. 10 The first eight vibration modal shapes of the simple wing

MODE 2

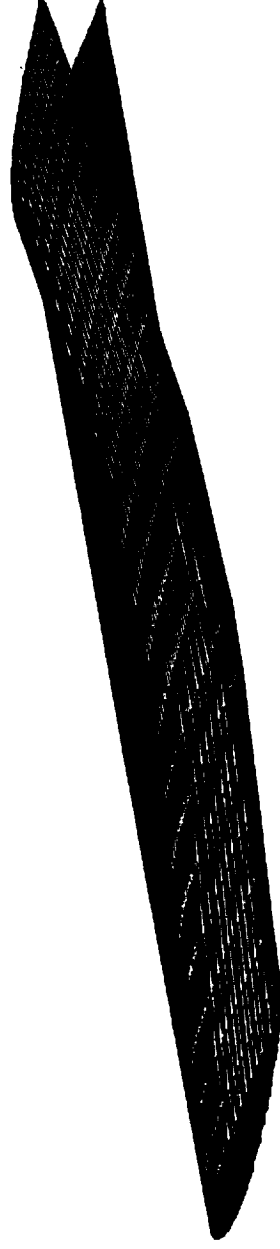


Fig. 10 (continued)

MODE 3

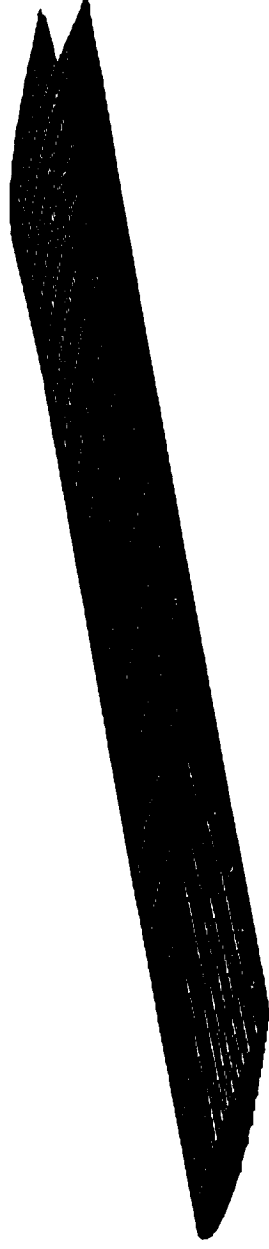


Fig. 10 (continued)

MODE 4

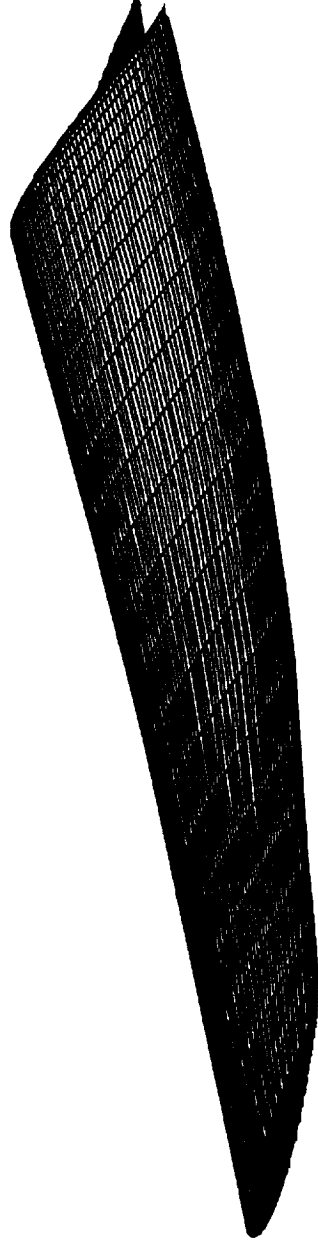


Fig. 10 (continued)

MODE 5

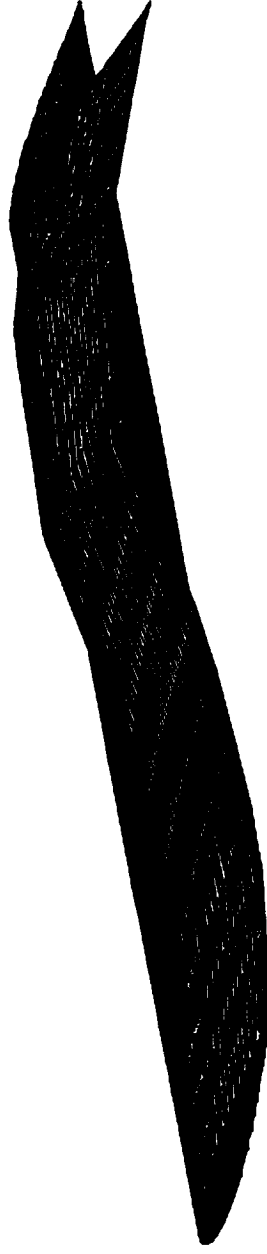


Fig. 10 (continued)

MODE 6



Fig. 10 (continued)

MODE 7



Fig. 10 (continued)

MODE 8

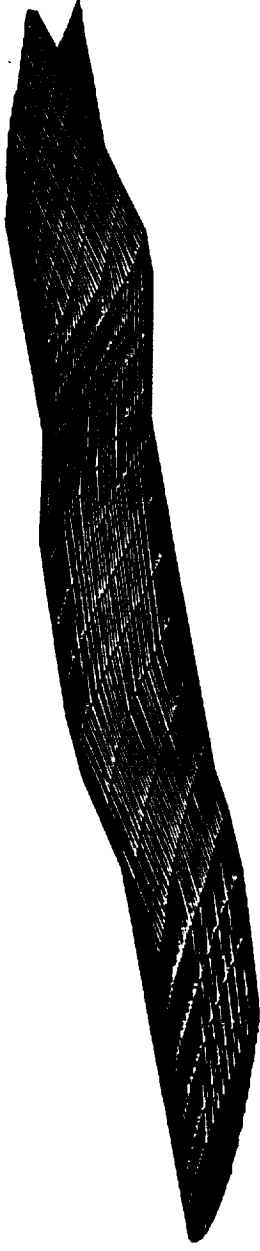


Fig. 10 (continued)

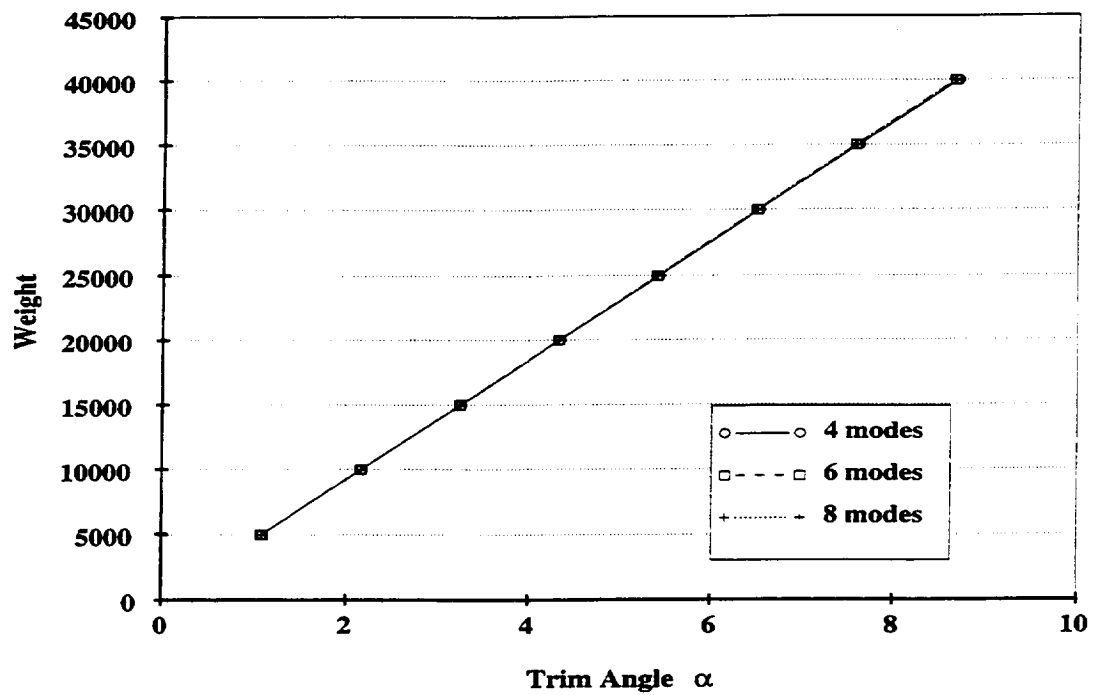


Figure 11. The effects of number of structural vibration modes in linear trim analysis

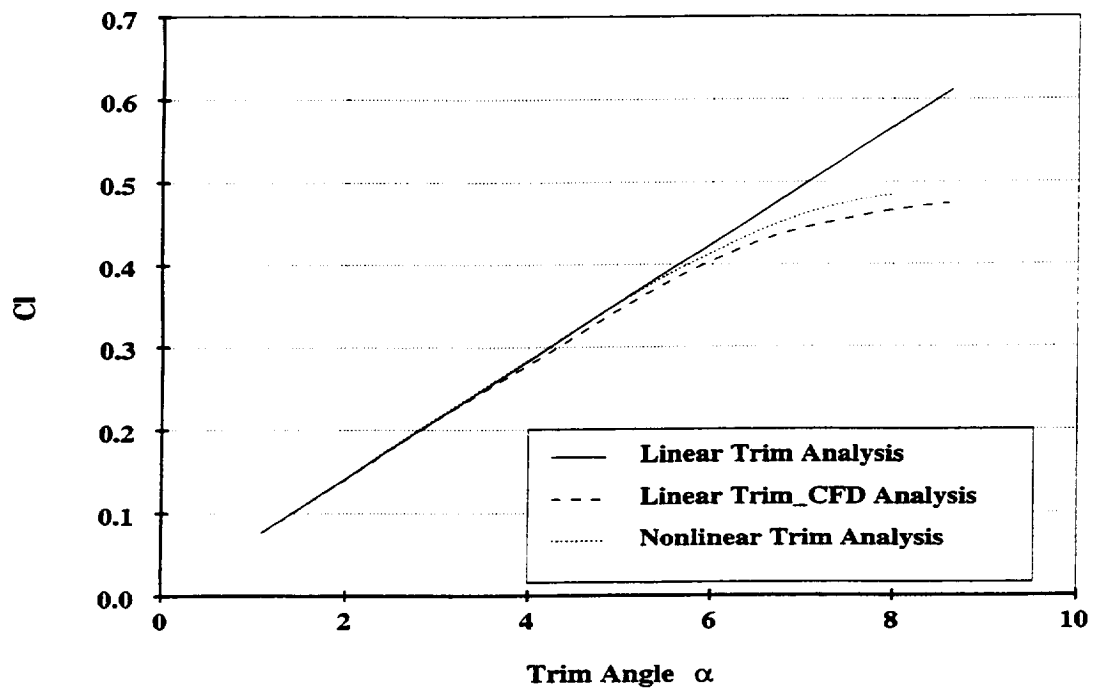


Figure 12. Lift coefficient of the simple wing as a function of the angle of attack

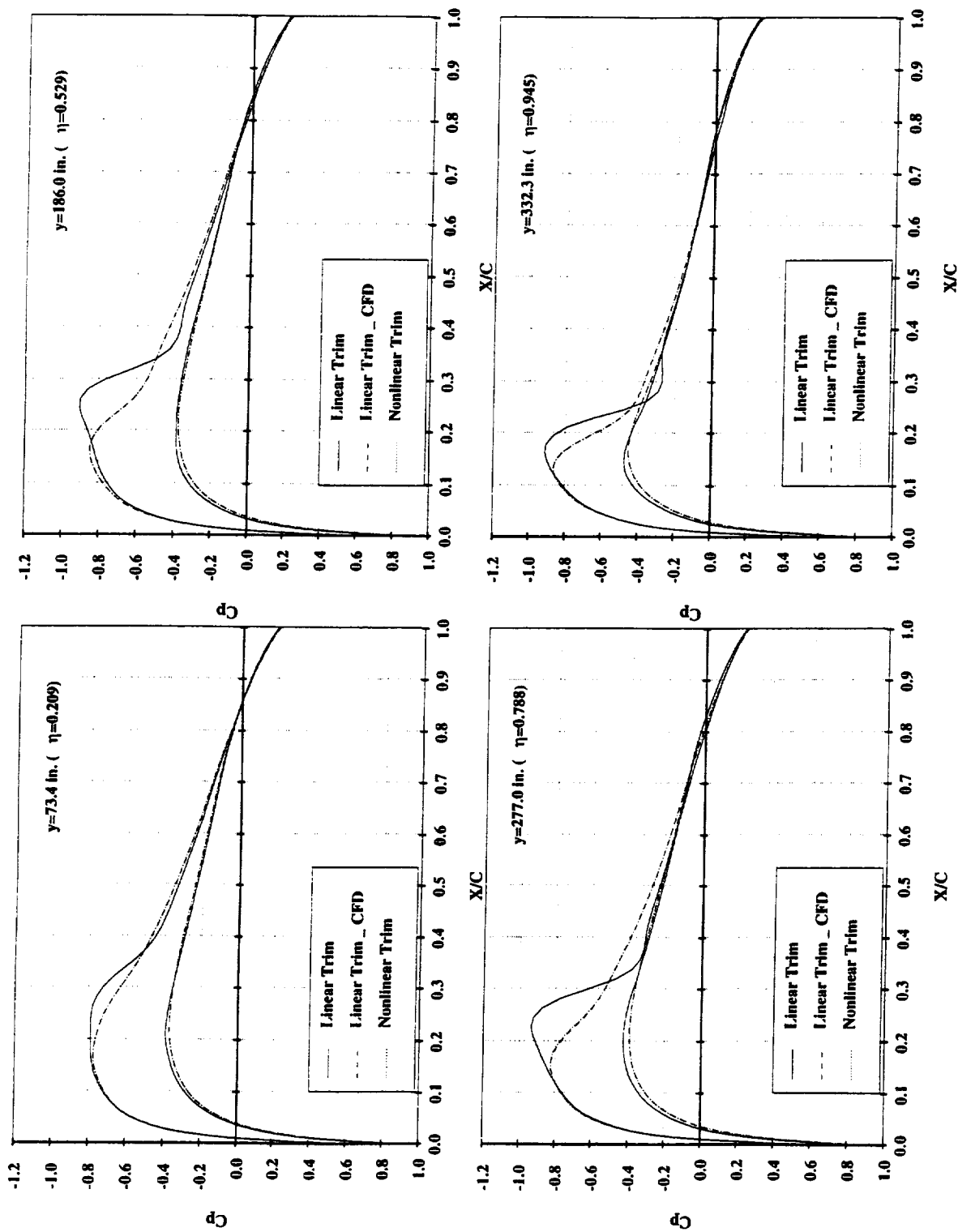


Figure 13. The pressure distributions at four spanwise locations of the simple wing at $\alpha = 2.158^\circ$

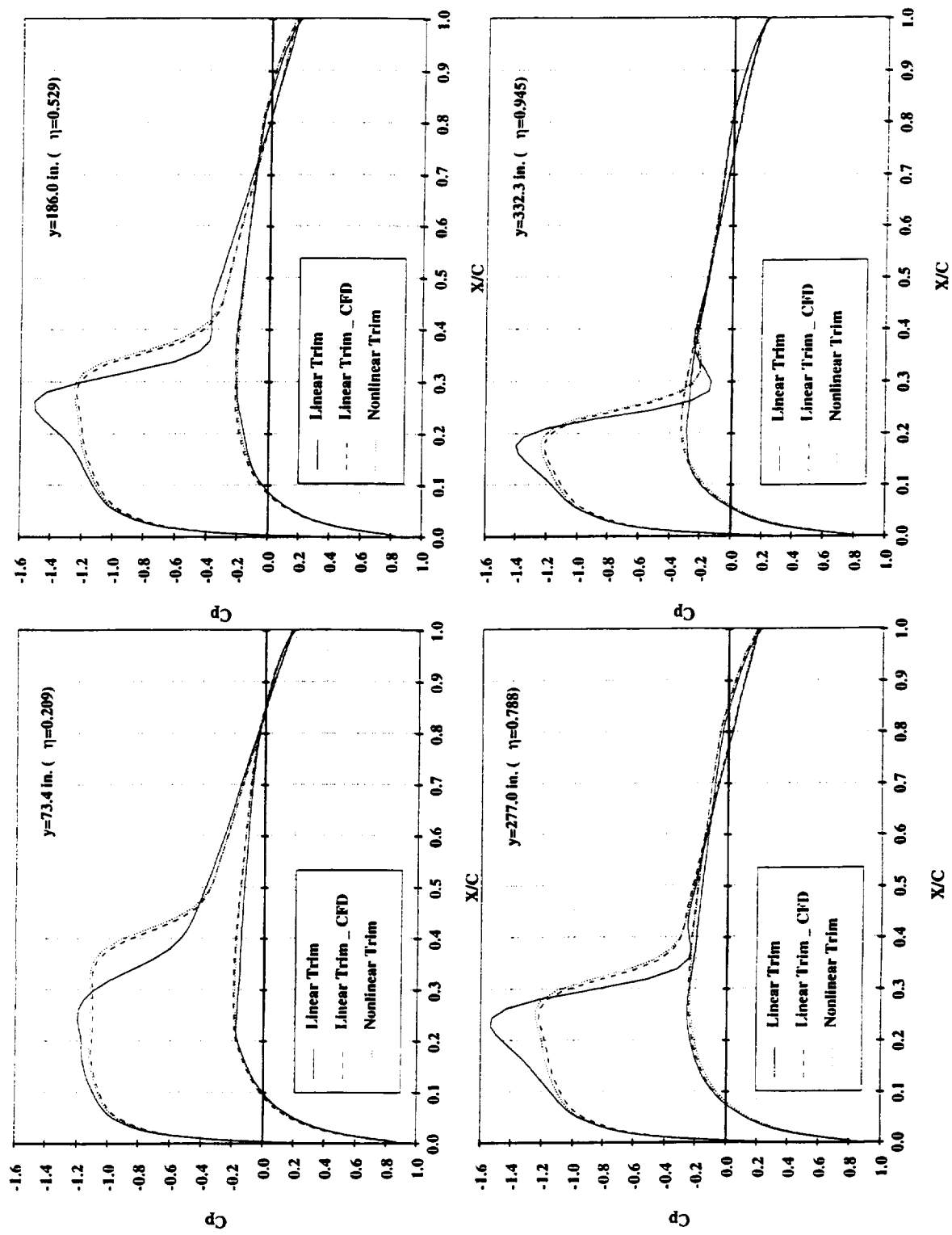


Figure 14. The pressure distributions at four spanwise locations of the simple wing at $\alpha = 5.463^\circ$

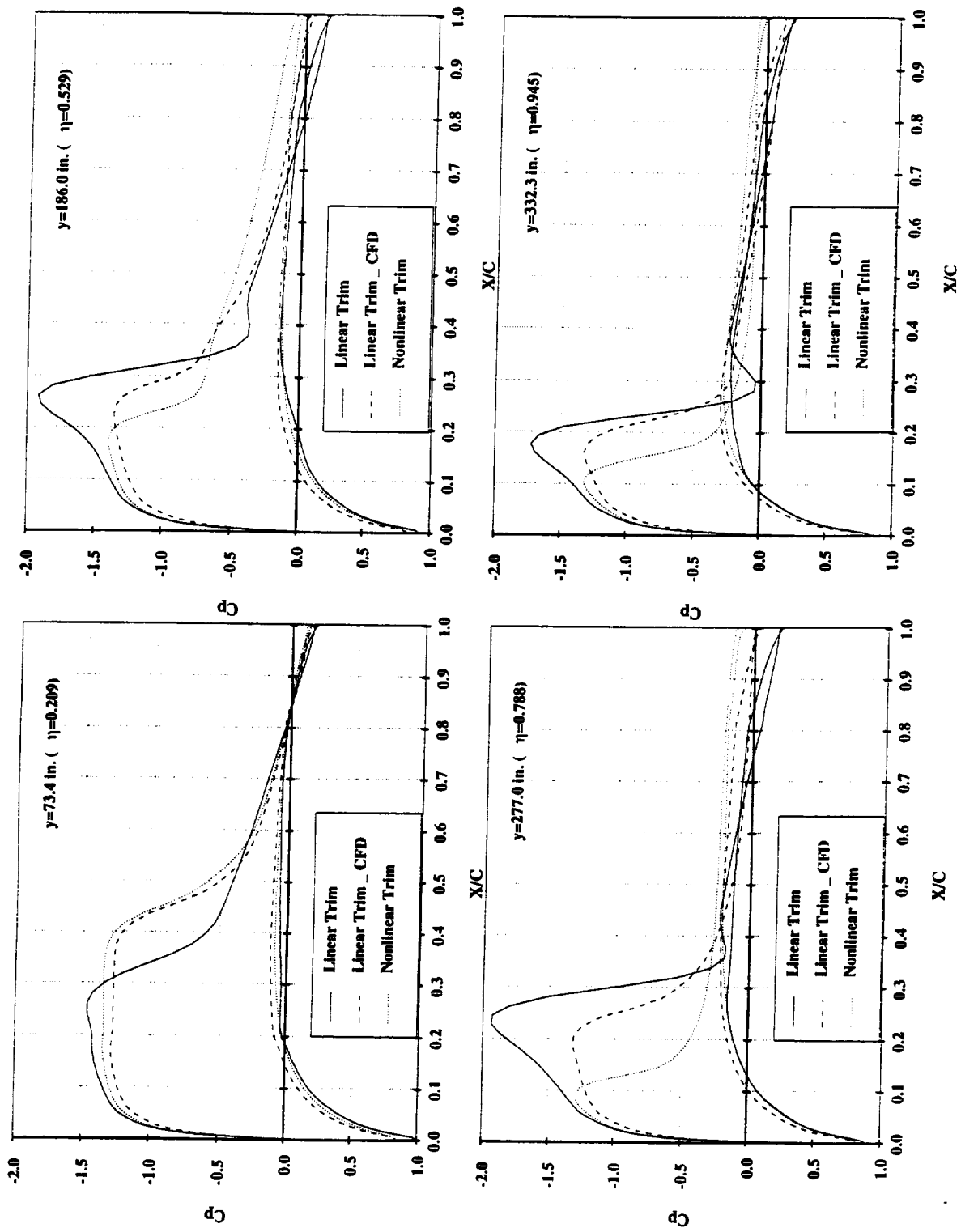


Figure 15. The pressure distributions at four spanwise locations of the simple wing at $\alpha=8.017^\circ$

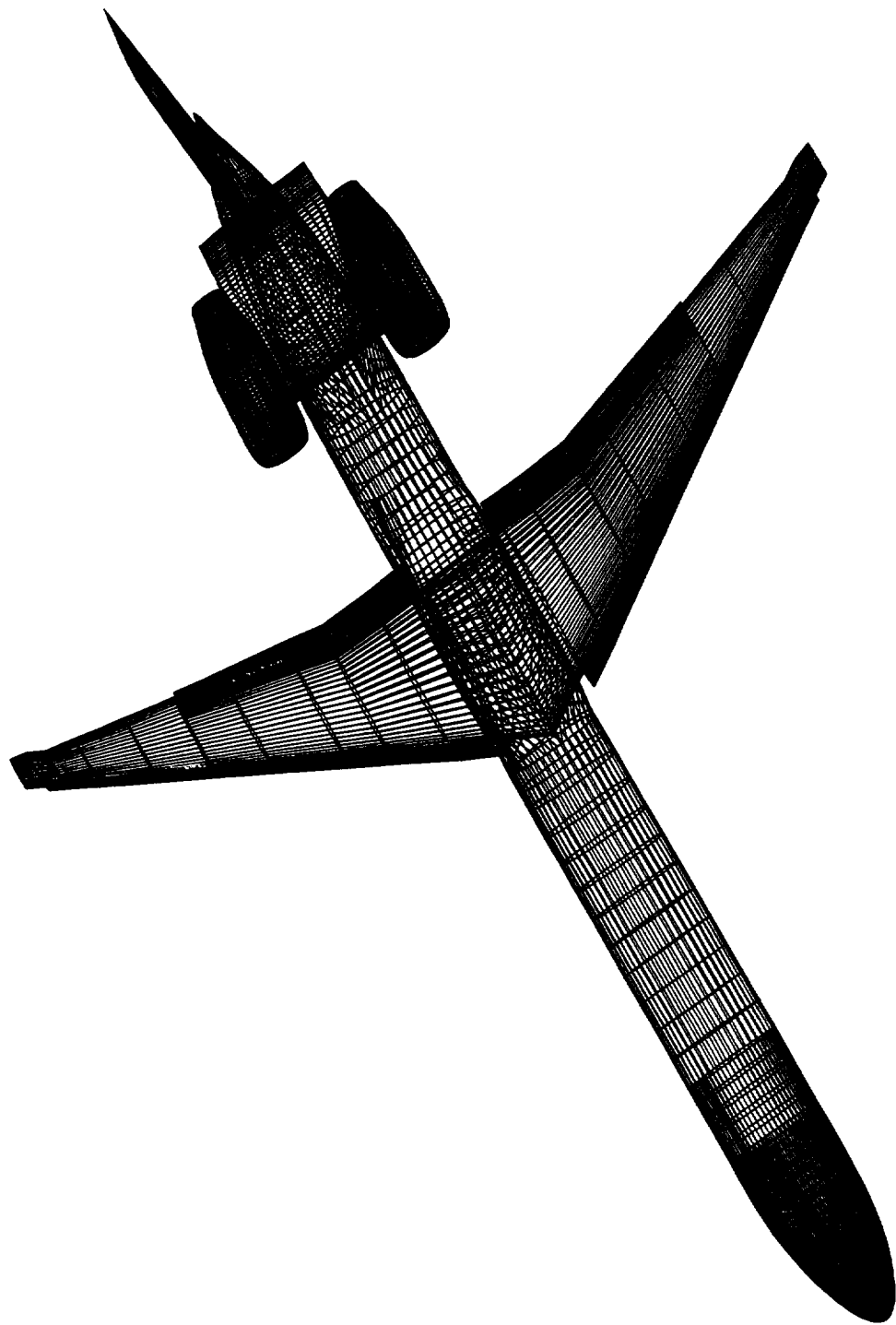


Fig 16. The MD-90 high lift configuration

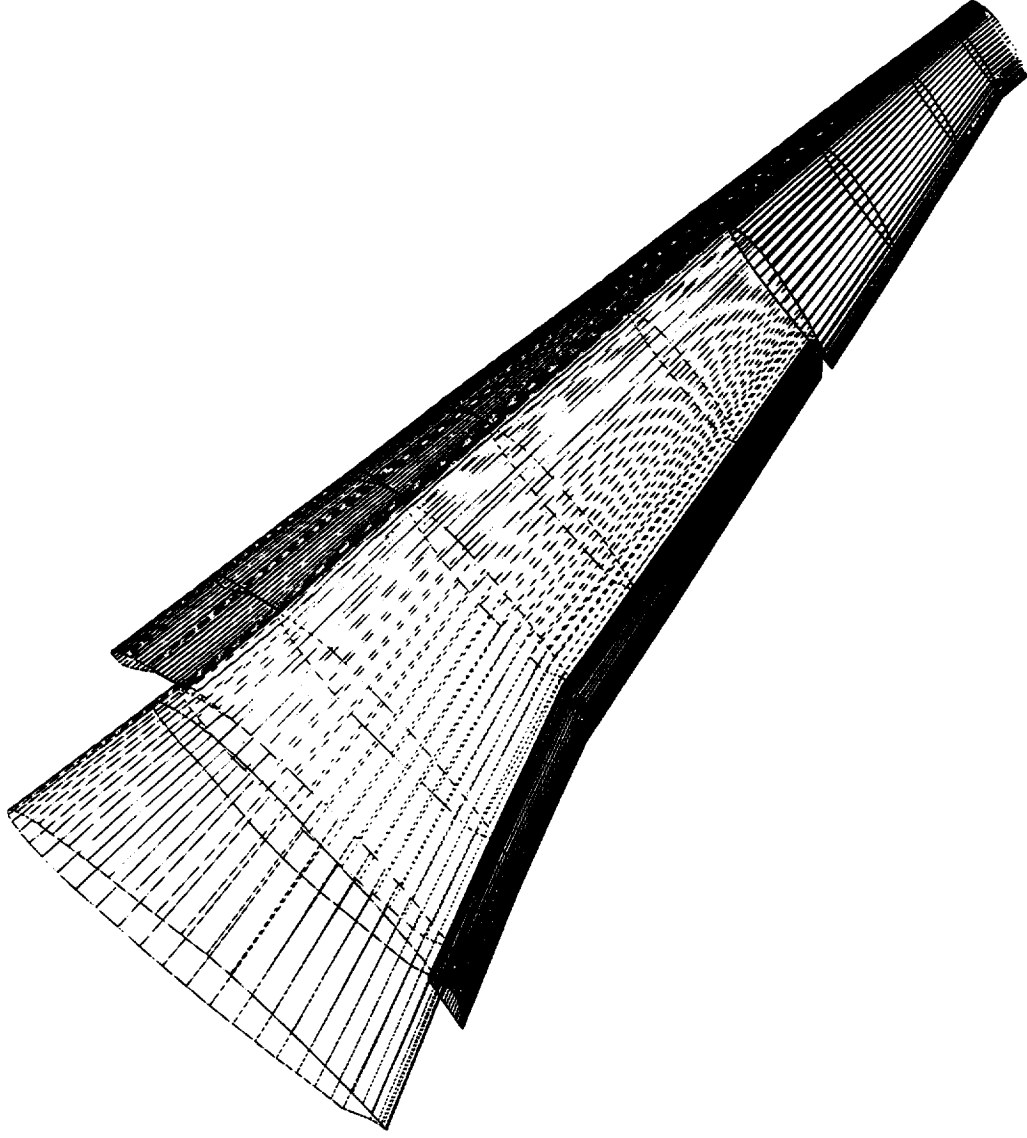


Fig 17. The MD-90 wing with high lift devices

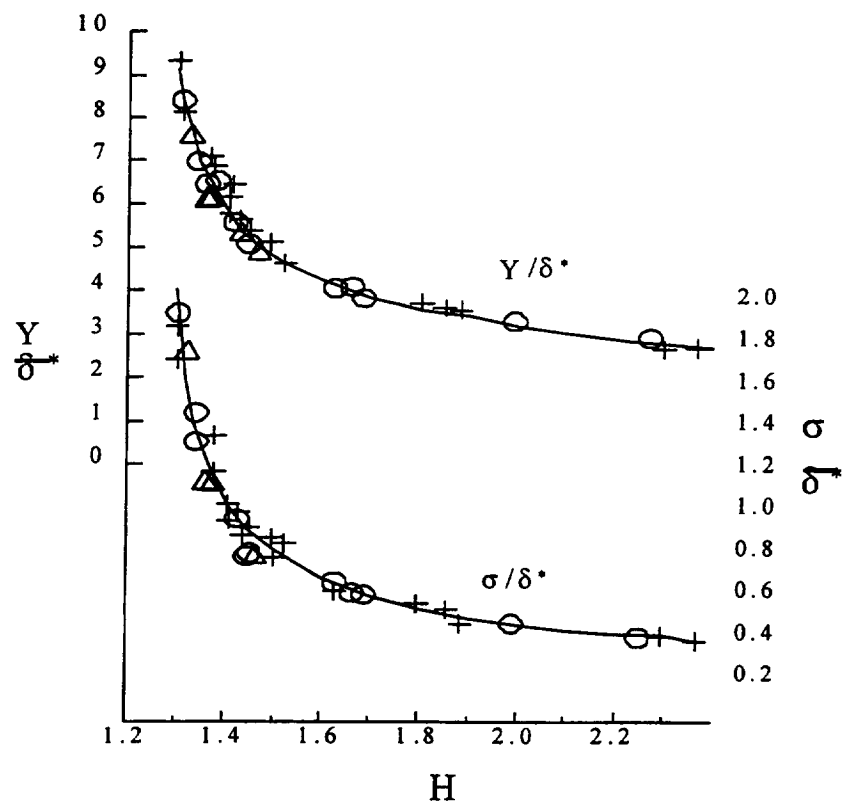
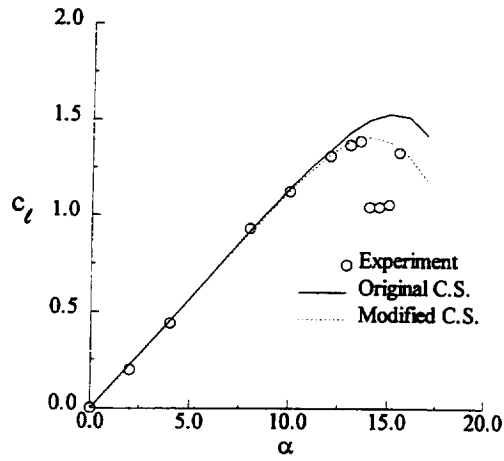
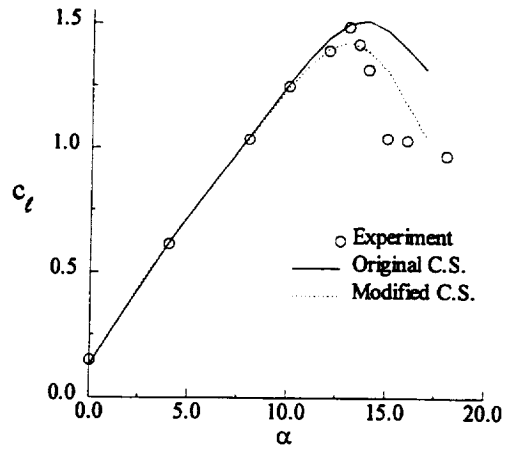


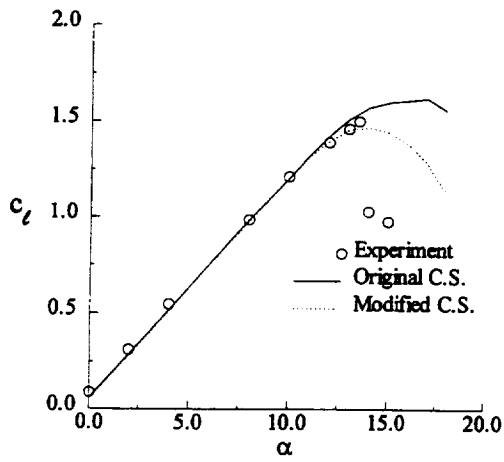
FIGURE 18 Variation of Y/δ^* and σ/δ^* with H according to the data of Fiedler and Head.



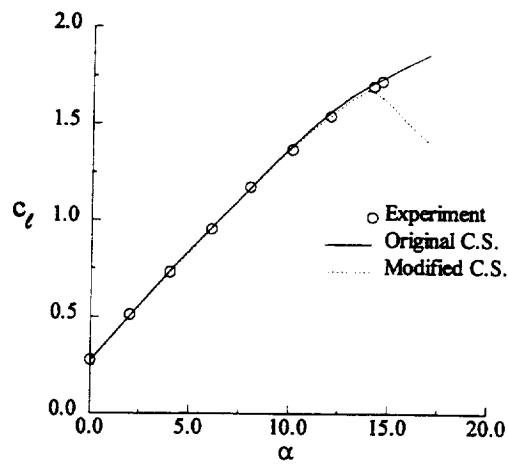
(a)



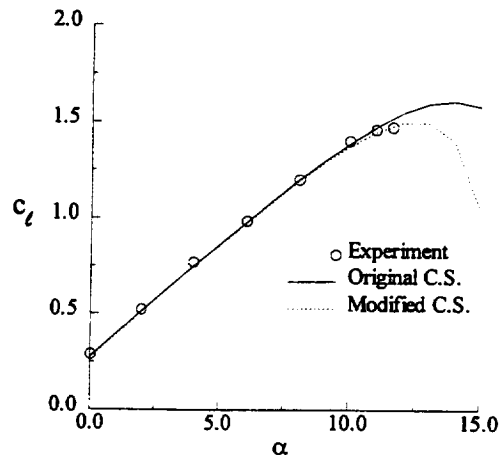
(b)



(c)

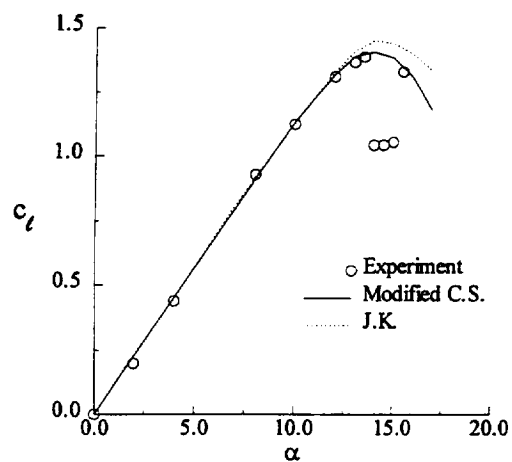


(d)

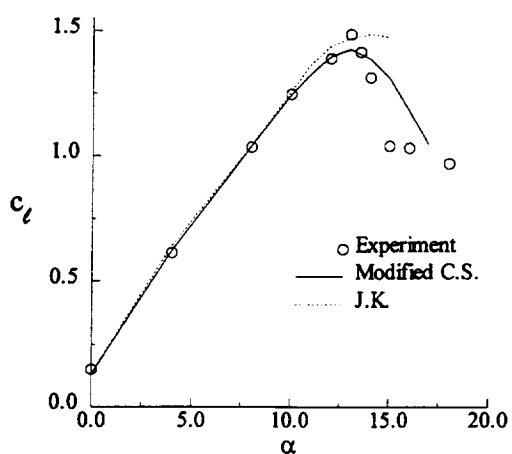


(e)

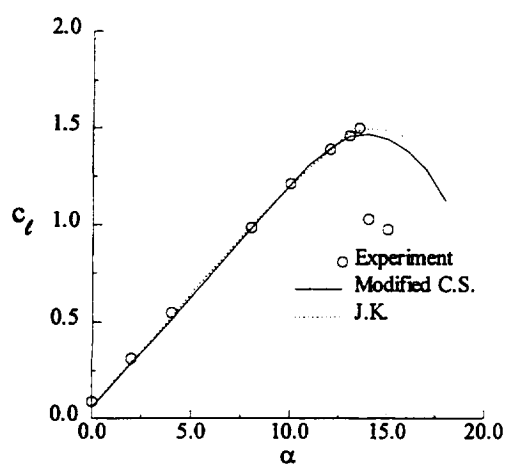
FIGURE 19 IBL results for the (a) NACA 0012 airfoil; (b) Wortmann airfoil; (c) Ames airfoil; (d) Boeing airfoil, $M_\infty = 0.2$; and (e) Boeing airfoil, $M_\infty = 0.3$.



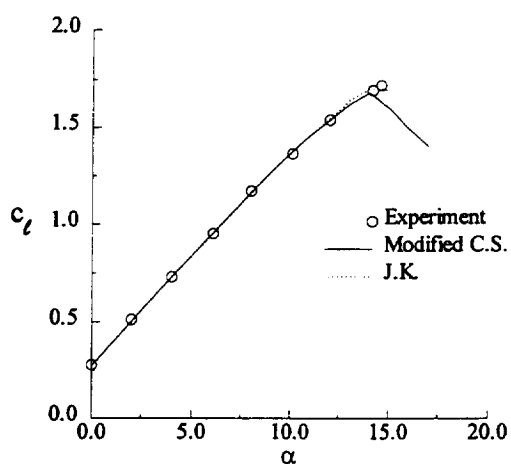
(a)



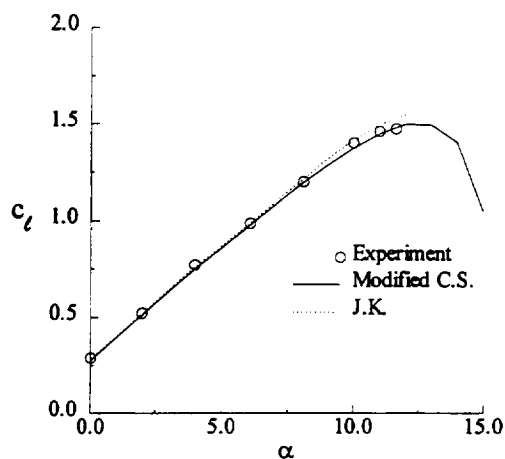
(b)



(c)

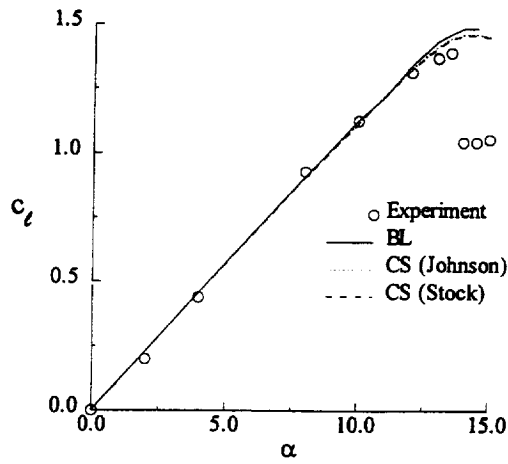


(d)

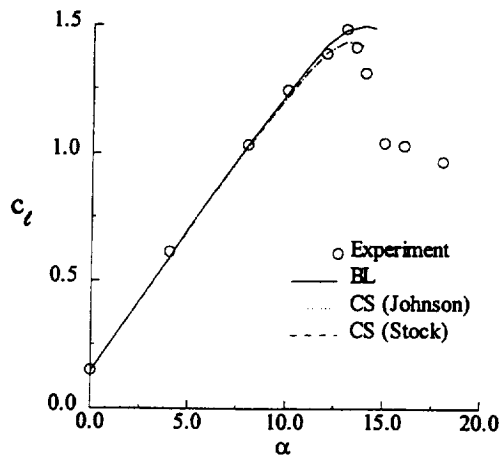


(e)

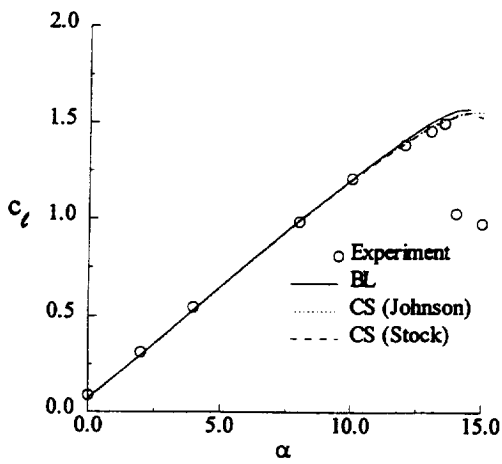
FIGURE 20. IBL results for the (a) NACA 0012 airfoil; (b) Wortmann airfoil; (c) Ames airfoil; (d) Boeing airfoil, $M_\infty = 0.2$; and (e) Boeing airfoil, $M_\infty = 0.3$.



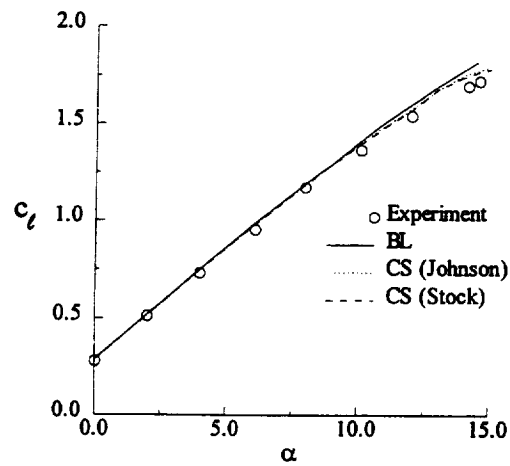
(a)



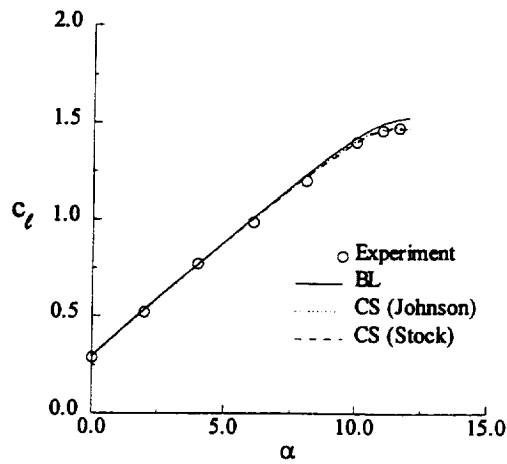
(b)



(c)



(d)



(e)

FIGURE 21. NS results for the (a) NACA 0012 airfoil; (b) Wortmann airfoil; (c) Ames airfoil; (d) Boeing airfoil, $M_\infty = 0.2$; and (e) Boeing airfoil, $M_\infty = 0.3$.

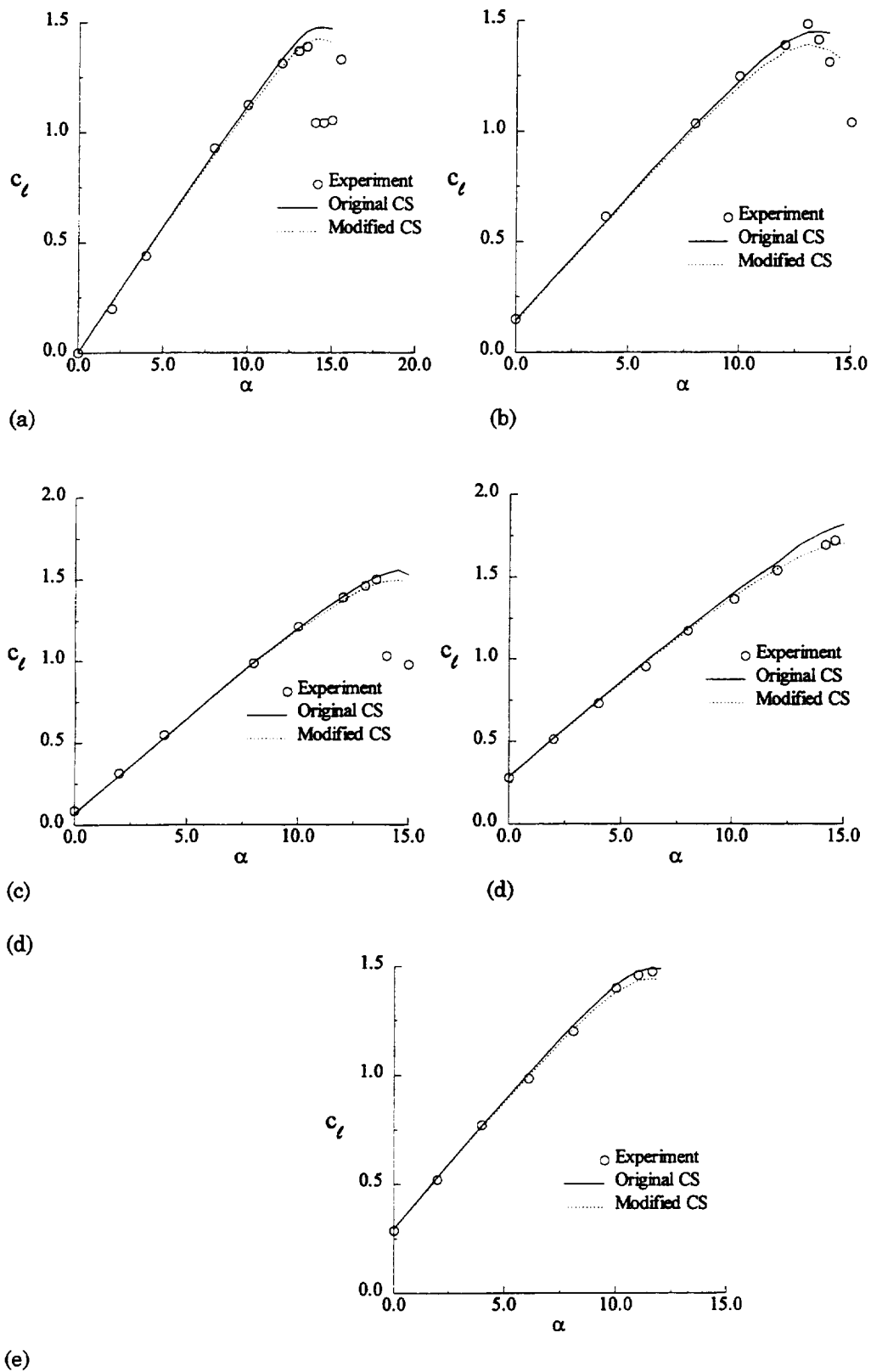
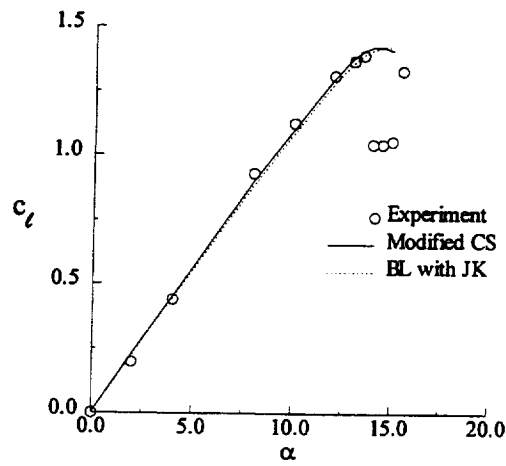
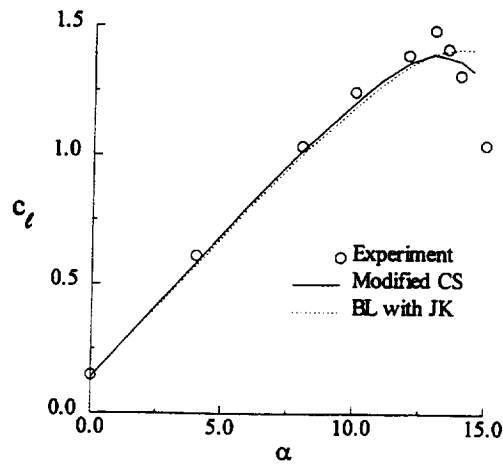


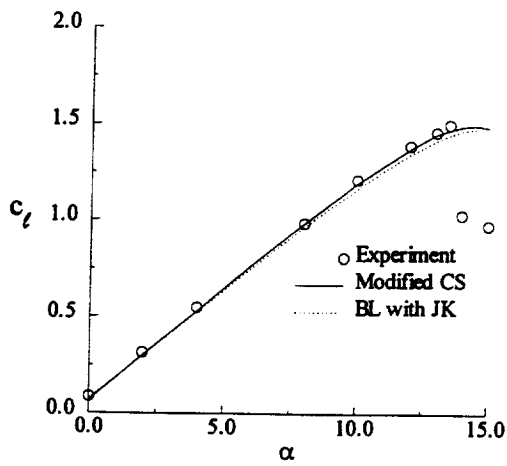
FIGURE 22 NS results for the (a) NACA 0012 airfoil; (b) Wortmann airfoil; (c) Ames airfoil; (d) Boeing airfoil, $M_\infty = 0.2$; and (e) Boeing airfoil, $M_\infty = 0.3$.



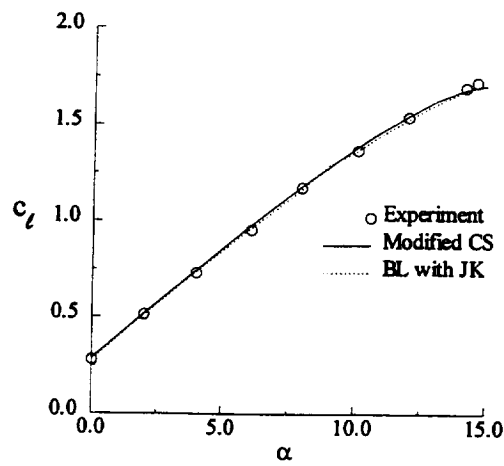
(a)



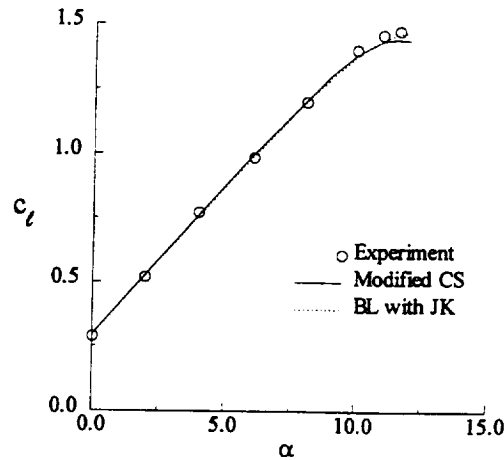
(b)



(c)



(d)



(e)

FIGURE 23 NS results for the (a) NACA 0012 airfoil; (b) Wortmann airfoil; (c) Ames airfoil; (d) Boeing airfoil, $M_\infty = 0.2$; and (e) Boeing airfoil, $M_\infty = 0.3$.

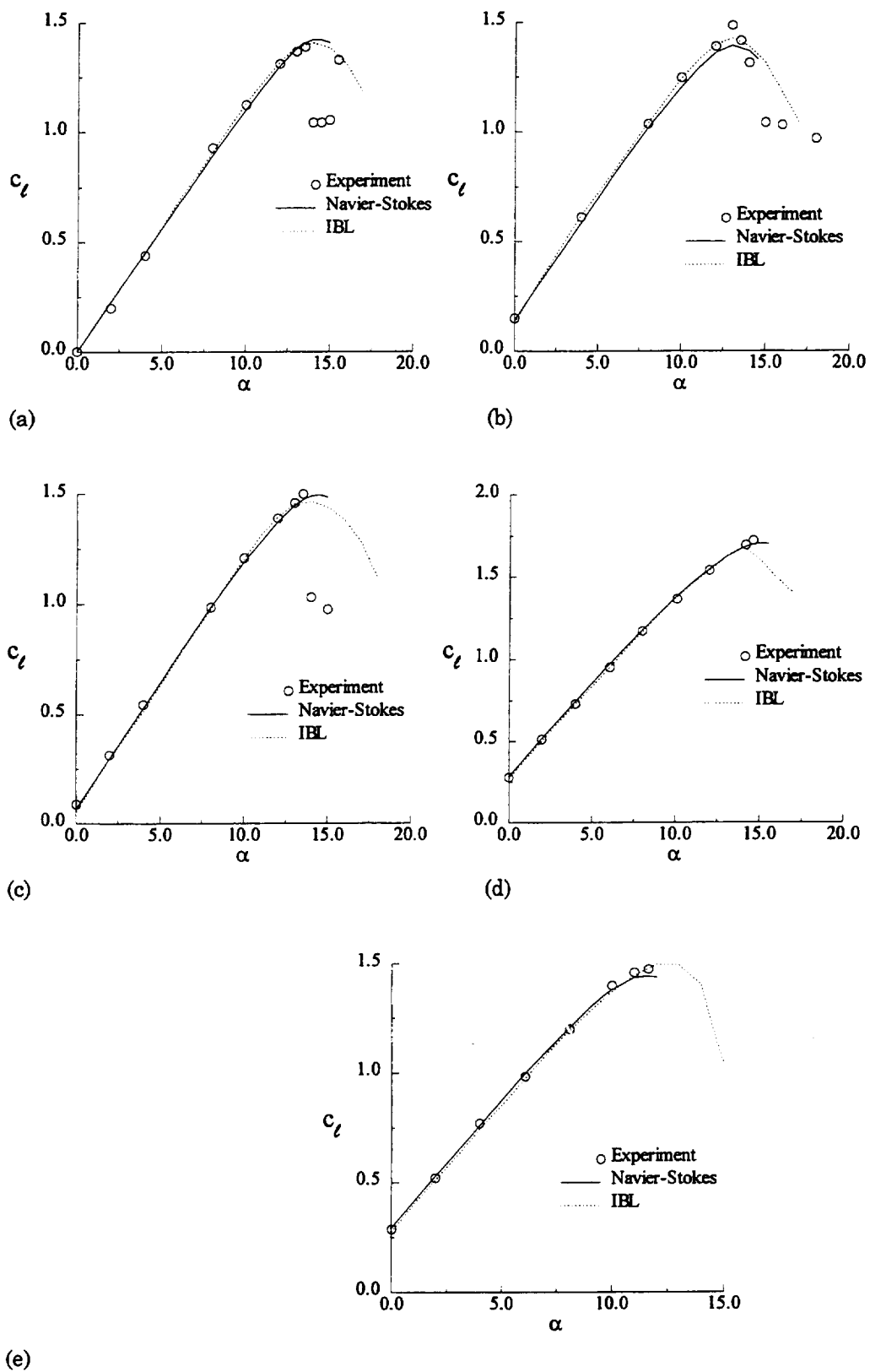


FIGURE 24 Comparison of NS and IBL results obtained with the modified CS model for the (a) NACA 0012 airfoil; (b) Wortmann airfoil; (c) Ames airfoil; (d) Boeing airfoil, $M_\infty = 0.2$; and (e) Boeing airfoil, $M_\infty = 0.3$.

